

Minimum-entropy constraints on galactic potentials

LEANDRO BERALDO E SILVA ^{1,2} MONICA VALLURI ¹ EUGENE VASILIEV ³ KOHEI HATTORI ^{4,5,1}
WALTER DE SIQUEIRA PEDRA,^{6,7} AND KATHRYNE J. DANIEL ²

¹*Department of Astronomy and Astrophysics, University of Michigan, Ann Arbor, MI, USA*

²*Steward Observatory and Department of Astronomy,*

University of Arizona, 933 N. Cherry Ave., Tucson, AZ 85721, USA

³*University of Surrey, Guildford, Surrey GU2 7XH, United Kingdom*

⁴*National Astronomical Observatory of Japan, 2-21-1 Osawa, Mitaka, Tokyo 181-8588, Japan*

⁵*The Institute of Statistical Mathematics, 10-3 Midoricho, Tachikawa, Tokyo 190-8562, Japan*

⁶*University of São Paulo, Institute of Mathematics and Computer Sciences, Av. Trab. São Carlense 400, 13566-590, São Carlos, SP, Brazil*

⁷*BCAM - Basque Center for Applied Mathematics, Mazarredo, 14. 48009 Bilbao, Spain*

ABSTRACT

A tracer sample in a gravitational potential, starting from a generic initial condition, phase-mixes towards a stationary state. This evolution is accompanied by an entropy increase, and the final state is characterized by a distribution function (DF) that depends only on integrals of motion (Jeans theorem). We present a method to constrain a gravitational potential where a sample is stationary by minimizing the entropy the sample would have if it were allowed to phase-mix in trial potentials. This method avoids assuming a known DF, and is applicable to any sets of integrals. We provide expressions for the entropy of DFs depending on energy, $f(E)$, energy and angular momentum, $f(E, L)$, or three actions, $f(\vec{J})$, and investigate the bias and fluctuations in their estimates. We show that the method correctly recovers the potential parameters for spherical and axisymmetric models. We also present a methodology to characterize the posterior probability distribution of the parameters with an Approximate Bayesian Computation, indicating a pathway for application to observational data. Using $N = 10^4$ tracers with 20%-uncertainties in the 6D coordinates, we recover the flattening parameter q of an axisymmetric potential with $\sigma_q/q \sim 10\%$.

Keywords: Galactic dynamics — Dark matter — Milky Way halo

1. INTRODUCTION

The gravitational potential is a fundamental aspect of any galaxy. It determines orbits for its stars and, afterall, the light distribution we observe in optical images of all kinds of galaxies. In the case of the Milky Way (MW), we can precisely measure 6D coordinates for millions of stars with Gaia (Gaia Collaboration et al. 2016) in combination with spectroscopic surveys such as APOGEE (Majewski et al. 2017), LAMOST (Cui et al. 2012), GALAH (De Silva et al. 2015) and DESI-MWS (Cooper et al. 2023). With theoretical modelling, this wealth of data can be translated into a detailed picture

of the Galaxy’s mass distribution. Of particular interest is the MW’s dark matter (DM) halo shape, which may constrain different scenarios for its composition (see e.g. Valluri et al. 2022). Since this component is not directly observed, one needs to infer its mass distribution from stars’ positions and kinematics.

A non-exhaustive list of methods to recover the underlying potential using a tracer sample includes: the virial theorem and its variants (Zwicky 1933; Bahcall & Tremaine 1981; Watkins et al. 2010), Jeans modelling (e.g. Rehemtulla et al. 2022), the “orbital roulette” (Beborodov & Levin 2004), the marginalization over an arbitrary number of distribution function (DF) components (Magorrian 2014), the generating-function method of Tremaine (2018), the minimization of the entropy of tidal streams (Peñarrubia et al. 2012; Sanderson et al.

2015), the “orbital pdf” method of Han et al. (2016); Li et al. (2024), Orbital Torus Imaging (Price-Whelan et al. 2021) and the DF fitting via Maximum-Likelihood (e.g. McMillan & Binney 2012, 2013; Deason et al. 2021).

In all these methods, further assumptions are required besides the information contained in the observed dataset. For instance, for tracers described by a DF, one needs to assume that they constitute a system in dynamical equilibrium. Otherwise, any potential is consistent with a DF describing a non-stationary system (McMillan & Binney 2012; Green et al. 2023). As another example, when modelling tidal streams, the equilibrium assumption is replaced by an equally strong one, that the debris were initially localized in phase space.

From the Jeans theorem, the DF of a system in equilibrium can be written as a function of integrals of motion only, reducing the 6D phase-space to 3D or less (Binney & Tremaine 2008). For instance, isotropic spherical systems can be described by a DF $f = f(E)$, where E is the star’s energy, while for anisotropic spherical systems we can assume $f = f(E, L)$, where L is the magnitude of the angular momentum. In general, samples in realistic galactic potentials normally require three integrals of motion. In practice, this dimension reduction is fundamental for a more efficient use of data.

Assuming a DF that depends on less integrals than required, i.e. a dimension reduction too severe, delivers incorrect results. On the other hand, one can assume a DF depending on more integrals than required, but this is not the most efficient use of data since it does not reduce the dimensions as much as possible. Thus, adopting three integrals is generally a good compromise between generality and efficiency.

Among all integrals of motion, actions offer several advantages (despite the difficulties in estimating them in practice – see e.g. Sanders & Binney 2016): the transformation from phase-space coordinates (\vec{r}, \vec{v}) to angle-action coordinates $(\vec{\theta}, \vec{J})$ is canonical, thus $d\vec{r}d\vec{v} = d\vec{\theta}d\vec{J}$; actions are adiabatic invariants, i.e. they are conserved under slow changes in the potential; angles are restricted to $[0, 2\pi)$, and a system in equilibrium (phase-mixed) is simply described by a probability density function (**pdf**)¹ in action space $F(\vec{J}) = (2\pi)^3 f(\vec{J})$. With angle-action variables, the Hamiltonian depends only on the momenta, $H = H(\vec{J})$, and the angle-coordinates increase linearly with time $\vec{\theta} = \vec{\Omega}t + \text{const}$, where $\vec{\Omega} = \partial H / \partial \vec{J}$. The dynamics is thereby reduced to that of “free particles”.

In the action-based DF-fitting method developed by McMillan & Binney (2012, 2013) and further applied and improved by e.g. Ting et al. (2013); Trick et al. (2016); Hattori et al. (2021), the tracer population is assumed to be in equilibrium, and characterized by a DF $f(\vec{J})$. The MW potential is constrained by fitting functional forms for both the total potential and the tracer DF. If the potential is the only function of interest, one further marginalizes over the DF parameters. For instance, Hattori et al. (2021) adopt a model with 9 parameters for the potential and 7 parameters for the DF which are later marginalized over, similarly to other works employing this technique. A disadvantage of this method is that it assumes an analytic expression for the DF, which in reality is unknown.

The main goal of the current paper is to improve on this aspect, by not assuming any functional form for the DF – for other methods with this intent see e.g. Han et al. (2016), Li et al. (2024) for spherically symmetric potentials. This avoids the overhead of fitting the DF parameters and possible biases introduced by the chosen DF. Information on the DF is obtained through a non-parametric entropy estimate.

Consider a tracer sample in equilibrium, and described by an unknown DF $f(\vec{r}, \vec{v})$. As for any DF, we can define the so-called differential entropy as

$$S \equiv - \int f \ln f \, d^6 \vec{w}, \quad (1)$$

where $\vec{w} = (\vec{r}, \vec{v})$. This entropy is invariant for changes of variables, and it is thus the same if we change to angle-action variables evaluated in any potential. In the correct potential where the sample is in equilibrium, the DF $f(\vec{r}, \vec{v}) = f(\vec{\theta}, \vec{J})$ is uniform in $\vec{\theta}$. The entropy associated with the angle-variables is then maximum, and to keep S invariant, the entropy associated with the actions must be minimum. This can be easily shown if $f(\vec{\theta}, \vec{J}) = \mathcal{F}(\vec{\theta})F(\vec{J})$, i.e. for a separable DF, in which case the entropy is just the sum of the entropies in action and angle spaces – in particular, for the fully phase-mixed sample $\mathcal{F}(\vec{\theta}) = (2\pi)^{-3}$. In Appendix A, we show that a similar idea also applies to non-separable DFs, which can always be separated in terms of conditional pdf’s, $f(\vec{\theta}, \vec{J}) = \mathcal{F}(\vec{\theta}|\vec{J})F(\vec{J})$. We then conclude that the correct potential is recovered by minimizing a quantity involving the entropy of the marginal pdf $F(\vec{J})$.

This quantity is actually the entropy of the future final DF describing the sample if it were allowed to phase-mix in each trial potential. This final DF would be a different (and unknown) function of actions in each trial potential. Since actions are conserved, we estimate this final entropy right away for each potential, with no need to wait for phase-mixing, and the true potential is the one

¹ We reserve the term DF and the notation $f()$ to the probability density function in 6D, and the term pdf and notation $F()$ to probability density functions of integrals of motion.

with minimum entropy. We also show that the same method is applicable to any sets of integrals, provided they respect the symmetry requirements of the problem. While one might try to fit potentials by instead maximizing an entropy in angle-space, in Appendix B we discuss why this is not expected to work.

Our approach is related to the minimum-entropy estimates of semi-parametric models (Wolsztynski et al. 2005), where the potential is the parametric part and the pdf is the non-parametric one. In Sec. 2 we describe the general formalism, starting from the action-based DF-fitting method and showing how it is extended by our method. Sec. 3 presents the expressions for the entropy estimator in the assumption-free (6D) case and in cases where the DF is a (unknown) function of integrals of motion. Sec 4 shows the physical basis of the method, investigates the bias and variance of the entropy estimates for DFs depending only on integrals, and apply a bias correction. In Sec. 5 we use a fixed sample that is phase-mixed in a given potential to illustrate that the entropy of the sample, estimated using integrals in different potentials, is minimum at the true potential. In Sec. 6 we demonstrate through actual fits that our method recovers the true parameters of a simple spherical potential, and of a flattened axisymmetric potential. We discuss our results in Sec. 7 and summarize in Sec. 8. The mathematical basis of the method is presented in Appendix A.

2. GENERAL FORMALISM

In the DF-fitting method, where an analytical function is assumed for $f(\vec{J})$, one starts defining the likelihood $\mathcal{L}_i(\vec{w}_i|\vec{p})$ for a star to have coordinates $\vec{w}_i \equiv (\vec{r}_i, \vec{v}_i)$. For simplicity, assume a full-sky sample in the absence of any selection function or observational errors – the full treatment is presented by e.g.: McMillan & Binney (2013); Hattori et al. (2021). In this case,

$$\mathcal{L}_i(\vec{w}_i|\vec{p}) = f_i(\vec{w}_i|\vec{p}), \quad (2)$$

where $f(\vec{w}|\vec{p}) = f(\vec{J}|\vec{p})$ is the modelled tracer population's DF, assumed here to be properly normalized. In this context, the parameters \vec{p} to be optimized describe the potential and the DF. The sample joint likelihood is $\mathcal{L} = \prod_{i=1}^N \mathcal{L}_i$, and the log-likelihood to be maximized is

$$\ln \mathcal{L}(\vec{w}|\vec{p}) = \sum_{i=1}^N \ln f_i, \quad (3)$$

with trial potentials entering the fit through the actions.

The formalism above is developed in the context of the DF-fitting method where an analytic DF is assumed. From now on, we shift to the minimum-entropy method

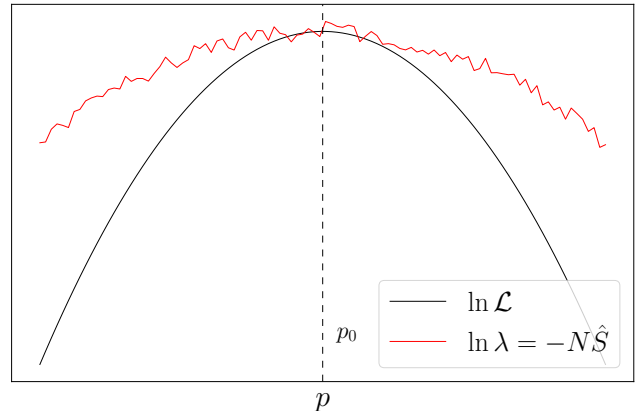


Figure 1. Illustrative scheme comparing the log-likelihood $\ln \mathcal{L}$ with the quantity used to find its maximum, $\ln \lambda$. Although being different quantities, on average they both peak at the same value p_0 and have the same value at the peak.

presented here, and in the remainder of this work \vec{p} encapsulates only parameters for the potential. With the Monte Carlo principle, the differential entropy, Eq. (1), can be estimated using a sample of f as

$$\hat{S} = -\frac{1}{N} \sum_{i=1}^N \ln \hat{f}_i, \quad (4)$$

where \hat{f}_i is an estimate² of $f(\vec{w}_i|\vec{p})$, as detailed in Sec. 3. Comparison of Eqs. (3) and (4) suggests defining

$$\ln \lambda(\vec{p}) \equiv -N \hat{S}(\vec{p}). \quad (5)$$

Despite appearances, $\ln \lambda(\vec{p})$ is not a log-likelihood for two reasons. First, the expectation value of Eq. (3), $\langle \ln \mathcal{L} \rangle$, does not involve Eq. (1), but

$$\langle \ln \mathcal{L} \rangle = -NH(f_0, f), \quad (6)$$

where

$$H(f_0, f) = -\int f_0 \ln f \, d\vec{w} \quad (7)$$

is the cross-entropy, \vec{p}_0 are the *true* parameters and $f_0 = f(\vec{w}|\vec{p}_0)$. Note that $H(f_0, f)$ is minimum for $f = f_0$, illustrating that the maximum likelihood happens at the true parameters (e.g. Akaike 1992). Thus, Eqs. (3) and (5) are only equivalent at the best fit model, i.e. $\ln \lambda(\vec{p}_0) \sim \ln \mathcal{L}(\vec{p}_0)$. Second, $\ln \lambda$ is not a smooth function of the parameters \vec{p} as required by its interpretation as a log-likelihood, but it is noisy since it is based on entropy estimates, rather than the actual entropy. However, as we demonstrate in practice in Sec. 6,

² For any quantity X we denote its estimate by \hat{X} .

and on mathematical grounds in Appendix A, on average $\ln \lambda$ has its maximum at \vec{p}_0 , and can be maximized to find the best fit model – see Fig. 1 for an illustration.

The maximum-likelihood principle is then replaced by a minimum-entropy one. As illustrated in Fig. 1, fluctuations in $\ln \lambda$ can lead to misidentifying the best fit model, and some smoothing is required to avoid that. In this paper, we estimate the entropy with the k^{th} -Nearest-Neighbor method (kNN, Leonenko et al. 2008), and we smooth out $\ln \lambda$ by averaging over several realizations of the data and by taking $k > 1$ – see Sec. 4.4. After identifying the best fit model by maximizing $\ln \lambda$, we perform an Approximate Bayesian Computation to sample the posterior and get confidence intervals for the parameters, as described in Sec. 6.

Although in this paper we do not consider any selection effects or a realistic survey footprint with geometric cuts, these are fundamental aspects for the applicability of the method to real data. With real data, we do not have a sample of the DF $f(\vec{w})$ assumed in equilibrium. Rather, we have a sample of the DF

$$f_S(\vec{w}) = \frac{f(\vec{w})\mathbb{S}(\vec{r})}{A}, \quad (8)$$

where $\mathbb{S}(\vec{r})$ is the selection function encapsulating the footprint and spatial dependencies within it, and $A = \int f(\vec{w})\mathbb{S}(\vec{r}) d^6\vec{w}$ is a normalization constant. Replacing in Eq. (1), we have

$$S = - \int \left(\frac{A}{\mathbb{S}(\vec{r})} f_S \right) \ln \left(\frac{A}{\mathbb{S}(\vec{r})} f_S \right) d^6\vec{w},$$

which is now a weighted differential entropy. This might make it difficult to estimate the entropy S , since the original estimators we discuss in Sec. 3 are intended to use samples of f . However, if the selection function $\mathbb{S}(\vec{r})$ is known, the estimating method can be adapted to provide S given samples of f_S – see Ajgl & Šimandl (2011).

In this paper, we consider ideal full-sky samples with no selection effects, and set $A = \mathbb{S}(\vec{r}) = 1$. Having presented the general formalism, we now present expressions to estimate the entropy in general and in particular cases of DFs only depending on integrals of motion.

3. ENTROPY ESTIMATORS

We start by defining the entropy of a DF, $f(\vec{w})$. Instead of Eq. (1), we modify the entropy definition as

$$S \equiv - \int f \ln \left(\frac{f}{\mu} \right) d^6\vec{w}, \quad (9)$$

where μ is such that the argument in $\ln(f/\mu)$ is dimensionless, e.g. if $[f] = \text{length}^{-3} \text{velocity}^{-3}$, it is convenient to use coordinates normalized by their dispersions

$\sigma_{w_1}, \dots, \sigma_{w_6}$, defining $w'_1 = w_1/\sigma_{w_1}, \dots, w'_6 = w_6/\sigma_{w_6}$. In this case, $\mu = |\Sigma|^{-1}$, where $|\Sigma| = \sigma_{w_1} \dots \sigma_{w_6}$, and with $f'(\vec{w}') = |\Sigma|f(\vec{w})$:

$$S = - \int f' \ln f' d^6\vec{w}' = - \int f \ln(|\Sigma|f) d^6\vec{w}. \quad (10)$$

For estimators with an isotropic kernel such as the kNN discussed below, this normalization works as to “isotropize” the coordinates, whereas the entropy is made invariant by an appropriate change of variables. Another advantage of the definition (9) is that it allows us to accommodate densities of states when using pdf’s of integrals of motion, as shown below.

Eq. (10) is the invariant entropy we start from in this section, and from which we transform coordinates for the cases where the DF is a function of integrals of motion only. For a sample of N points, it can be estimated as

$$\hat{S} = -\frac{1}{N} \sum_{i=1}^N \ln \hat{f}'_i, \quad (11)$$

where \hat{f}'_i is an estimate of $f'(\vec{w}'_i)$, and several density estimators can be employed – see Silverman (1986). However, to estimate the entropy with Eq. (11), a few estimators are optimal (Beirlant et al. 1997; Leonenko et al. 2008) – for a comparison of different methods in N -body simulations, see Beraldo e Silva et al. (2017). The latter work demonstrated, in particular, the high accuracy of the Fokker-Planck modelling of the collisional relaxation, later confirmed on rigorous theoretical grounds by Fouvry et al. (2021). More recently, Modak & Hamilton (2023) also used this entropy estimator in a study of the eccentricity distribution of wide binaries.

Here we use the kNN estimator, where

$$\hat{f}'_i = \frac{1}{(N-1)e^{-\psi(k)}V_d D_{ik}^d}, \quad (12)$$

and

$$V_d = \pi^{d/2}/\Gamma(d/2+1) \quad (13)$$

is the volume of the d -dimensional unit-radius hypersphere, $D_{ik} = \sqrt{(\vec{r}'_i - \vec{r}'_k)^2 + (\vec{v}'_i - \vec{v}'_k)^2}$ is the Euclidean phase-space distance of particle i to its k^{th} nearest neighbor, and $\psi(x)$ is the digamma function³.

For two general distributions f_0 and f , we also re-define their cross-entropy as

$$H(f_0, f) \equiv - \int f_0 \ln \left(\frac{f}{\mu} \right) d^6\vec{w}. \quad (14)$$

³ In particular, $\psi(1) = -\gamma \approx -0.57722$ (Euler-Mascheroni constant) and, for large k : $\psi(k) \approx \ln(k-1/2) \rightarrow \hat{f}'_i \approx k/(NV_d D_{ik}^d)$.

Note that, in general, it is possible to estimate $H(f_0, f)$ even if the samples of f_0 and f have different sizes N and M , respectively. Eq. (14) is estimated as

$$\hat{H} = -\frac{1}{N} \sum_{i=1}^N \ln \hat{\xi}'_i, \quad (15)$$

where

$$\hat{\xi}'_i = \frac{1}{M e^{-\psi(k)} V_d D_{ik}^d}, \quad (16)$$

and now D_{ik} is the distance between point i of the f_0 -sample to its k -nearest neighbor *in the f -sample* (Leonenko et al. 2008). We can interpret $\hat{\xi}'_i$ as an estimate of f at the point i of the f_0 -sample. In this paper, we restrict to samples of equal sizes, so $M = N$. As explained in 6.1, when exploring the posterior distribution of the parameters, f_0 will describe the best fit model obtained in a previous step, and f will describe each trial model.

Eqs. (11) and (15), with Eqs. (12) and (16) respectively plugged in, converge in probability to the true entropies, under weak conditions on the underlying DFs (e.g. Leonenko et al. 2008; Biau & Devroye 2015; Lombardi & Pant 2016). The k -nearest neighbors identification is also fast since it can be optimized with KD-trees.

As explained in Sec. 1, the method developed here assumes the sample is phase-mixed in a given potential, and also considers the entropy the sample would have if evolved until phase-mixed in a trial potential. In the next subsections, we show explicit expressions for cases where the DF only depends on integrals of motion, as required by the Jeans theorem for phase-mixed samples. In Appendix A, we provide more detailed derivations.

3.1. Isotropic spherical system, $f = f(E)$

For isotropic spherical systems in equilibrium, we can write $f(\vec{w}) = f(E)$, where $E = v^2/2 + \phi(r)$ and $\phi(r)$ is the potential. In this case, Eq. (10) reduces to

$$S_E = - \int F(E) \ln \left[\frac{|\Sigma| F(E)}{g(E)} \right] dE, \quad (17)$$

where

$$F(E) = f(E)g(E) \quad (18)$$

is the pdf in energy space and

$$g[E|\phi(r)] = (4\pi)^2 \int_0^{r_m(E)} r^2 \sqrt{2[E - \phi(r)]} dr \quad (19)$$

is the density of states, with $r_m(E)$ being the radius where $\phi = E$. If σ_E is a typical energy dispersion, we define $E' = E/\sigma_E$, and estimate S_E , Eq. (17), as

$$\hat{S}_E = -\frac{1}{N} \sum_{i=1}^N \ln \left[\frac{\hat{F}'_i(E'_i)}{\mu(E_i)} \right], \quad (20)$$

where $\mu(E) = \sigma_E |\Sigma|^{-1} g[E|\phi(r)]$. We estimate $\hat{F}'_i(E'_i)$, the energy pdf, with $d = 1$ and $D_{ik} = |E'_i - E'_k|$ in Eq. (12). If it is convenient to write the density of states in terms of the normalized energy and angular momentum, we can replace $g[E|\phi(r)] = \sqrt{\sigma_E} g[E'|\phi(r)/\sigma_E]$.

3.2. Anisotropic spherical system, $f = f(E, L)$

For anisotropic spherical systems with a DF $f(\vec{w}) = f(E, L)$, where $L = v_t r$ and $v_t^2 = v_\theta^2 + v_\varphi^2$ in spherical coordinates (r, θ, φ) , Eq. (10) reduces to

$$S_{EL} = - \int F(E, L) \ln \left[\frac{|\Sigma| F(E, L)}{g(E, L)} \right] dE dL, \quad (21)$$

where the pdf for energy and angular momentum is

$$F(E, L) = f(E, L)g(E, L), \quad (22)$$

and the density of states is

$$g[E, L|\phi(r)] = 8\pi^2 L T_r [E, L|\phi(r)]. \quad (23)$$

The period of radial motion $T_r [E, L|\phi(r)]$ is given by

$$T_r [E, L|\phi(r)] = 2 \int_{r_{\text{per}}}^{r_{\text{apo}}} \frac{dr}{\sqrt{2[E - \phi(r)] - L^2/r^2}}, \quad (24)$$

with r_{per} and r_{apo} being the peri- and apo-center distances. Defining $(E', L') = (E/\sigma_E, L/\sigma_L)$, we estimate

$$\hat{S}_{EL} = -\frac{1}{N} \sum_{i=1}^N \ln \left[\frac{\hat{F}'_i(E'_i, L'_i)}{\mu(E_i, L_i)} \right], \quad (25)$$

where $\mu(E, L) = \sigma_E \sigma_L |\Sigma|^{-1} g[E, L|\phi(r)]$, and for the pdf we plug in Eq. (12) with $d = 2$ and $D_{ik} = \sqrt{(E'_i - E'_k)^2 + (L'_i - L'_k)^2}$. If desired, we replace $g[E, L|\phi(r)] = (\sigma_L^2/\sigma_E) g[E', L'|\phi(r')/(\sigma_L \sqrt{\sigma_E})]$, where $r' = (\sqrt{\sigma_E}/\sigma_L)r$.

3.3. Generic integrable potential, $f = f(\vec{J})$

For realistic galactic potentials, assuming that most orbits are regular or weakly chaotic, we may compute approximate actions with e.g. the Stäckel approximation (Binney 2012). In this context, a system in dynamical equilibrium is described by a pdf in action space

$$F(\vec{J}) = (2\pi)^3 f(\vec{J}), \quad (26)$$

where \vec{J} are three actions. Thus, Eq. (10) reduces to

$$S_{\vec{J}} = - \int F(\vec{J}) \ln \left[\frac{|\Sigma| F(\vec{J})}{(2\pi)^3} \right] d\vec{J}. \quad (27)$$

The simplicity of Eq. (27), in comparison to Eqs. (17)-(19) or Eqs. (21)-(24), illustrates the advantages of using action-based DFs instead of other integrals of motion. Defining new actions \vec{J} normalized by their dispersions ($\sigma_{J_1}, \sigma_{J_2}, \sigma_{J_3}$), we have

$$\hat{S}_{\vec{J}} = -\frac{1}{N} \sum_{i=1}^N \ln \left[\frac{\hat{F}_i'(\vec{J}_i')}{\mu} \right], \quad (28)$$

where $\mu = (2\pi)^3 \sigma_{J_1} \sigma_{J_2} \sigma_{J_3} |\Sigma|^{-1}$, and for the pdf we plug in Eq. (12) with $d = 3$ and $D_{ik} = \sqrt{|\vec{J}_i' - \vec{J}_k'|^2}$.

The same expressions apply to the cross-entropy estimates, Eqs. (15)-(16), *mutatis mutandis*.

Having presented the expressions in general and for DFs depending only on integrals of motion, in the next section we illustrate the physical basis of the method, as well as investigate the bias and fluctuation in these estimates. For that, we use a model with explicit expressions for $f(E)$, $g(E)$ and for the actions.

4. THE ISOCHRONE MODEL

To illustrate the accuracy of these entropy estimators and the physical basis of our method, we consider the Isochrone model (Henon 1959), whose potential is

$$\phi(r) = -\frac{GM}{b} \frac{1}{1 + \sqrt{1 + (r/b)^2}}, \quad (29)$$

where M is the total mass and b the scale length. The DF of a self-consistent sample is (see Binney & Tremaine 2008; Binney & Petrou 1985)

$$f(E) = \frac{1}{\sqrt{2}(2\pi)^3 (GMb)^{3/2}} \frac{\sqrt{\varepsilon}}{[2(1-\varepsilon)]^4} \times \left[27 - 66\varepsilon + 320\varepsilon^2 - 240\varepsilon^3 + 64\varepsilon^4 + 3(16\varepsilon^2 + 28\varepsilon - 9) \frac{\sin^{-1} \sqrt{\varepsilon}}{\sqrt{\varepsilon(1-\varepsilon)}} \right], \quad (30)$$

and the density of states, Eq. (19), is

$$g(E) = (2\pi)^3 \sqrt{GMb}^{5/2} \frac{(1-2\varepsilon)^2}{(2\varepsilon)^{5/2}}, \quad (31)$$

where $\varepsilon = -bE/(GM)$. The radial period is

$$T_r(E, L) = \frac{2\pi GM}{(-2E)^{3/2}}. \quad (32)$$

As for any spherical system, the azimuthal and latitudinal actions are $J_\varphi = L_z$ and $J_\theta = L - |L_z|$, respectively, and the radial action is

$$J_r = \frac{1}{\pi} \int_{r_{\text{per}}}^{r_{\text{apo}}} dr \sqrt{2E - 2\phi(r) - L^2/r^2}. \quad (33)$$

For the Isochrone potential,

$$J_r = \frac{GM}{\sqrt{-2E}} - \frac{1}{2} \left(L + \sqrt{L^2 + 4GMb} \right). \quad (34)$$

4.1. Entropy bias

We start evaluating the integral in Eq. (17) numerically with Eqs. (30)-(31), from $E_{\text{min}} = -0.5$ to $E_{\text{max}} = -10^{-8}$, with $G = M = b = 1$. We take this as the true entropy value, $S_{E, \text{true}}$ – thick solid grey line in Fig. 2 (upper panel). We generate self-consistent samples with different sizes N of this model with AGAMA (Vasiliev 2019), and integrate orbits for these samples for $50 \times \langle T_{\text{circ}} \rangle$, where T_{circ} is the period of circular motion. Fig. 2 (upper panel) shows the entropy estimates \hat{S}_{6D} (thin solid lines) at different times and for different N (colors), taking the nearest neighbor ($k = 1$). We recalculate $|\Sigma| = \sigma_{w_1} \dots \sigma_{w_6}$, renormalizing the coordinates at each time with the appropriate change of variables in Eq. (10). This provides better estimates than a fixed initial normalization, but the difference is small.

Since the initial sample is self-consistent with the potential, it is stationary and \hat{S}_{6D} should be conserved. We see that this is the case for all sample sizes, with larger fluctuations for smaller N . Furthermore, \hat{S}_{6D} is significantly biased with respect to the true value, and this bias is time-independent, except for minor fluctuations. In the bottom panel, the hexagons show the relative bias $\delta S_{6D} = (\langle \hat{S}_{6D} \rangle_t - S_{E, \text{true}}) / S_{E, \text{true}}$ as a function of N , where $\langle \hat{S}_{6D} \rangle_t$ is a time-average. Even for $N = 10^8$, \hat{S}_{6D} has a relative bias of $\approx 1\%$.

Fig. 2 (upper panel) shows the entropy estimates $\hat{S}_{\vec{J}}$, Eq. (28), i.e. assuming the DF is an unknown function of the actions (dashed lines). Since these are conserved, we only estimate $S_{\vec{J}}$ at $t = 0$. We see that $\hat{S}_{\vec{J}}$ produces a much smaller bias, due to the dimension reduction from 6D to 3D. The triangles in the bottom panel show that the bias stays below $\approx 1\%$ even for $N = 10^4$. Crosses and dots show the relative bias for \hat{S}_{EL} and \hat{S}_E , respectively. These are estimated with Eq. (20) for S_E , i.e. assuming the DF is an unknown function $f = f(E)$, and Eq. (25) for S_{EL} . We see that the bias is also significantly smaller than that of \hat{S}_{6D} .

Thus, we have shown that: \hat{S}_{6D} is appropriately conserved in the self-consistent model, but it is biased with respect to the true value by $\delta S / S_{E, \text{true}} \approx 5\%$ for $N = 10^4$, whereas in the space of integrals of motion the estimates recover the true entropy with $\delta S / S_{E, \text{true}} < 1\%$ for $N = 10^4$, and $\delta S / S_{E, \text{true}} \lesssim 0.01\%$ for $N = 10^8$.

4.2. Phase-mixing and entropy increase

Next we use the same initial samples and integrate orbits in the potential ($M = 3, b = 1$) for $50 \times \langle T_{\text{circ}} \rangle$, which is enough for the samples to relax, and estimate the entropy at several time-steps. Fig. 3 (upper panel) shows \hat{S}_{6D} ($\hat{S}_{\vec{J}}$) with solid (dashed) lines. Since the initial sample is not in dynamical equilibrium in the new

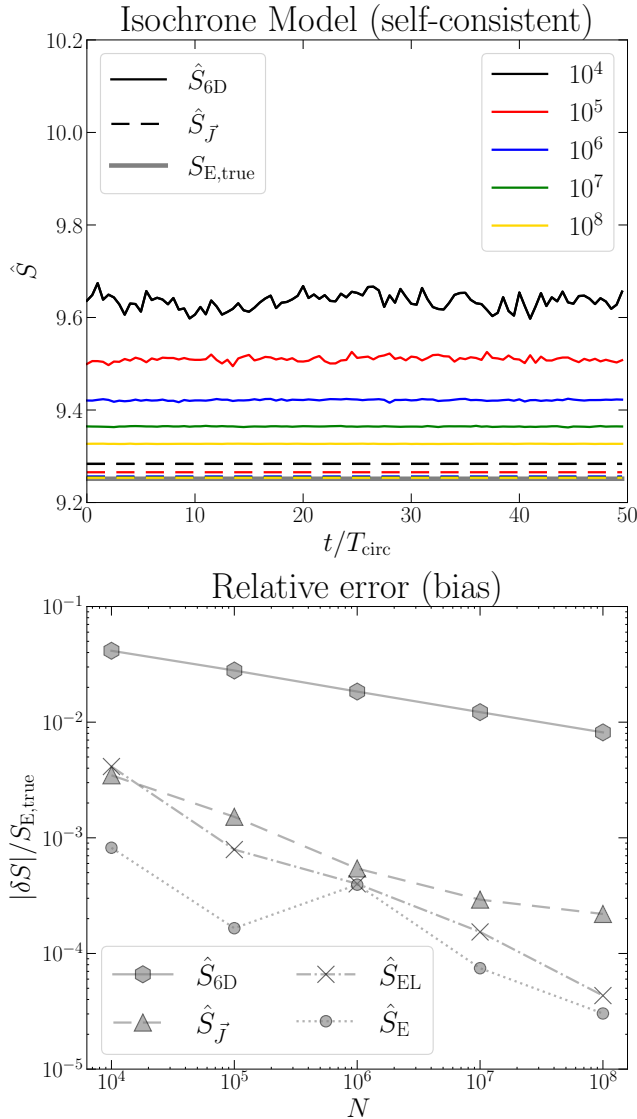


Figure 2. Upper panel: entropy estimates in 6D (solid) and assuming the DF is an unknown function $f(\vec{J})$ (dashed) for self-consistent samples of the Isochrone model, with different sample sizes (colors). The thick solid grey line shows the true value – numerical integral in Eq. (17). Bottom panel: relative error (bias) of \hat{S}_{6D} , $\hat{S}_{\vec{J}}$, \hat{S}_{EL} and \hat{S}_E . For a fixed sample size, estimates in lower dimensions are more accurate.

potential, it responds to the higher mass developing a radially biased velocity anisotropy, broadening the radial action distribution – see Fig. 4. The final DF is unknown, but it should respect the Jeans theorem, being a function $f(E, L)$, or $f(\vec{J})$. The thick solid grey line shows \hat{S}_{EL} for $N = 10^8$ in the new potential, which is the lower dimension allowed by the phase-mixed sample. Since we have shown that \hat{S}_{EL} has a negligible bias for $N = 10^8$, we take this as the true final entropy, $\hat{S}_{EL,\text{true}}$.

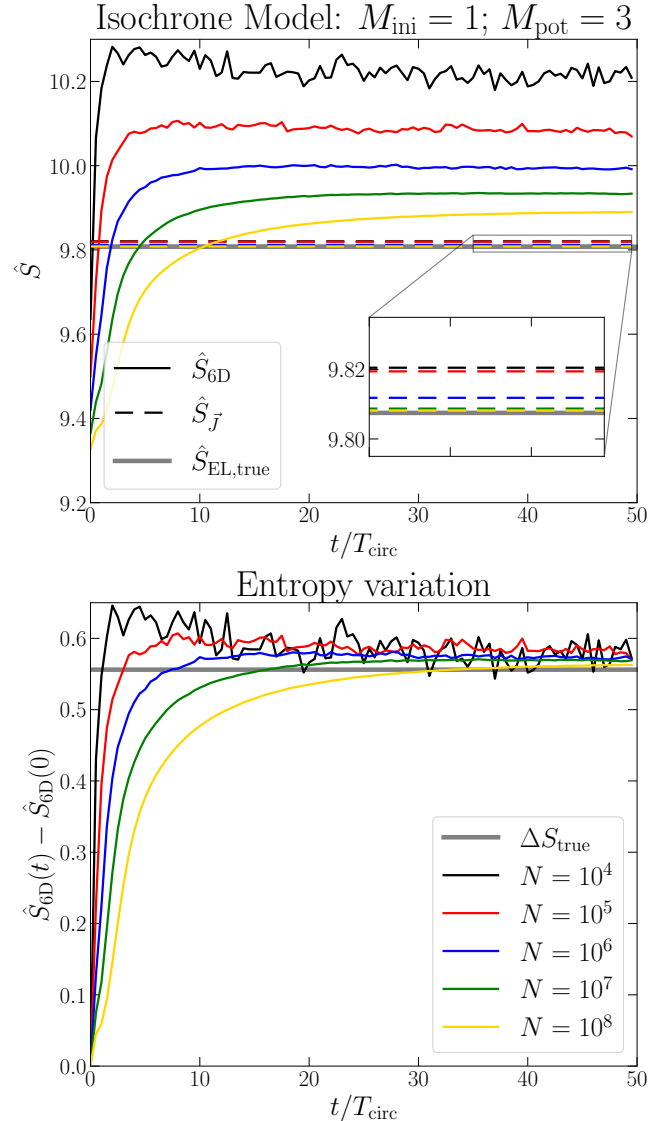


Figure 3. Top: entropy estimates in 6D (solid) and assuming $f = f(\vec{J})$ (dashed) for initial self-consistent samples of the Isochrone model with $M = 1$, but integrated in (and \vec{J} evaluated at) an Isochrone potential with $M = 3$. The thick solid grey line shows the entropy for a phase-mixed system with $f = f(E, L)$ and $N = 10^8$, considered as the true final entropy. Bottom: entropy variation $\Delta \hat{S} = \hat{S}_{6D}(t) - \hat{S}_{6D}(0)$ for different sample sizes, which approximately converges to $\Delta S_{\text{true}} = \hat{S}_{EL,\text{true}} - S_{E,\text{true}}$ for all samples.

Besides the biases with respect to the initial true entropy $S_{E,\text{true}}$ (see Fig. 2), Fig. 3 shows that the asymptotic values of $\hat{S}_{6D}(t \rightarrow \infty)$ in the new potential are also biased with respect to the true final value $\hat{S}_{EL,\text{true}}$. On the other hand, $S_{\vec{J}}$ is again much less biased. In both cases the bias decreases for larger N – see the inset plot.

Fig. 3 (bottom panel) shows $\Delta \hat{S}_{6D} = \hat{S}_{6D}(t) - \hat{S}_{6D}(0)$ (coloured) and the true entropy increase

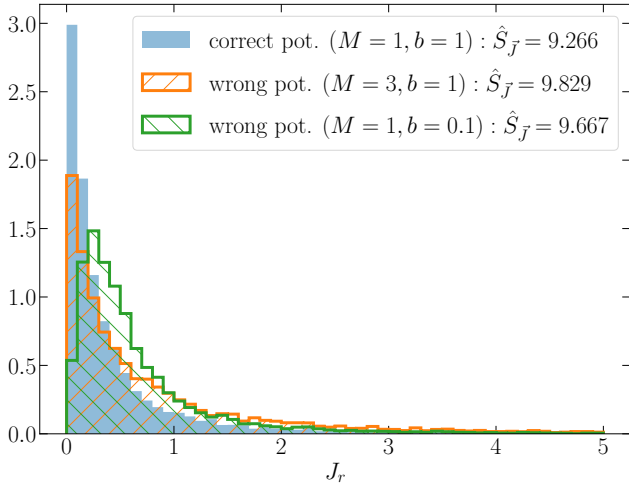


Figure 4. Histograms of the radial action for a self-consistent sample of an Isochrone model with $(M, b) = (1, 1)$, and actions evaluated in this model (“correct pot.”) and for $(M, b) = (3, 1)$ and $(M, b) = (1, 0.1)$. The J_r distribution is broader in the wrong potentials (where the original sample is not stationary), resulting in larger entropies (legend).

$\Delta S_{\text{true}} = \hat{S}_{\text{EL, true}} - S_{\text{E, true}}$ (thick grey). The final $\Delta \hat{S}_{6\text{D}}$ is similar for all sample sizes and it approximately converges to ΔS_{true} . This confirms that the bias is nearly independent of time and is thus nearly eliminated by calculating entropy variations, as previously done by Beraldo e Silva et al. (2017, 2019b,a).

Note that this orbit integration only serves to illustrate the continuous entropy increase for non-stationary samples in a given potential. From Jeans theorem, the final DF will be a function of integrals only, and since these are conserved, we can estimate the final entropy right away for the given sample with integrals evaluated in that potential.

Fig. 4 shows histograms of the radial action J_r for the fixed self-consistent sample of the Isochrone model $(M = 1, b = 1)$ with $N = 10^4$, and actions evaluated in this potential (“correct potential”), and for $(M = 3, b = 1)$ and $(M = 1, b = 0.1)$. Since J_φ and J_θ do not depend on the potentials in the spherical case, the final entropy is determined by the J_r distribution. We see that the histogram is narrower in the correct potential, in agreement with its lower $\hat{S}_{\mathcal{J}}$ value (legend).

4.3. Bias correction

If the bias of \hat{S} does not depend on the model parameters, it poses no problem for the minimum-entropy fits, since it only introduces an additive constant in \hat{S} . For a possibly model-dependent bias, we investigate it in more detail and test a prescription to suppress it.

It is known that taking the k^{th} neighbor for larger k increases the bias in the entropy estimate, but decreases its variance, a manifestation of the common bias-variance trade-off (e.g. Wasserman 2010). To investigate this, we generate 10^3 realizations of size- N self-consistent samples of the Isochrone model with $M = b = 1$. Then we calculate actions and $\hat{S}_{\mathcal{J}}$, Eq. (28), for each realization, normalizing the actions in each one. In this case we do not compare with $\hat{S}_{6\text{D}}$, thus we do not normalize physical coordinates by $|\Sigma|$, which would introduce unnecessary extra noise.

Fig. 5 (upper panel) shows the bias, i.e. the difference between the mean of the realizations and the true value, as a function of k for different sample sizes (full triangles). We confirm the increase in the bias for larger k , with $k = 10$ producing a $\sim 2\times$ larger bias than $k = 1$.

We investigate the correction proposed by Charzyńska & Gambin (2015), who suggest that the bias is essentially due to points near the edges of the distribution support. For these points, the hyper-sphere around the point (defined by the distance D_{ik} to the k -th neighbor) can have a fraction of its volume outside the support. This results in overestimating the volume, and Eq. (12) underestimating the DF for these points. When plugged into Eq. (11), this produces a positive bias, in accordance with our results – Figs. 2, 3 and 5. To compensate for this, Charzyńska & Gambin (2015) propose to add the following correction to the entropy estimate:

$$C = \frac{1}{N} \sum_{i=1}^N \ln \left(\frac{|v(\vec{w}_i, D_{ik}) \cap \text{supp}(W)|}{|v(\vec{w}_i, D_{ik})|} \right), \quad (35)$$

where $v(\vec{w}_i, D_{ik})$ is the volume around point \vec{w}_i , which is drawn from W , in d -dimensions.

It is hard to determine the support’s shape and to calculate the intersections in Eq. (35) in general, and Charzyńska & Gambin (2015) propose assuming a hyper-rectangular box for the support and a hyper-cubic box for the volume $v(\vec{w}_i, D_{ik})$, although their analysis restricted to $k = 1$. Assuming cubic boxes of side l_i , we correct for points such that $w_{j,i} > w_{j,\text{max}} - l_i/2$, or $w_{j,i} < w_{j,\text{min}} + l_i/2$, where $j = 1, \dots, d$, and calculate the volume fractions of the cube inside the rectangular box. Concisely, it results that

$$C = \frac{1}{N} \sum_{i=1}^N \sum_{j=1}^d \ln \left[\min \left(\frac{w_{j,\text{max}}}{l_i}, \frac{w_{j,i}}{l_i} + \frac{1}{2} \right) - \max \left(\frac{w_{j,\text{min}}}{l_i}, \frac{w_{j,i}}{l_i} - \frac{1}{2} \right) \right]. \quad (36)$$

After a few experiments, we settled a cube inscribed within the sphere of radius D_{ik} , i.e. $l_i = (2/\sqrt{d})D_{ik}$.

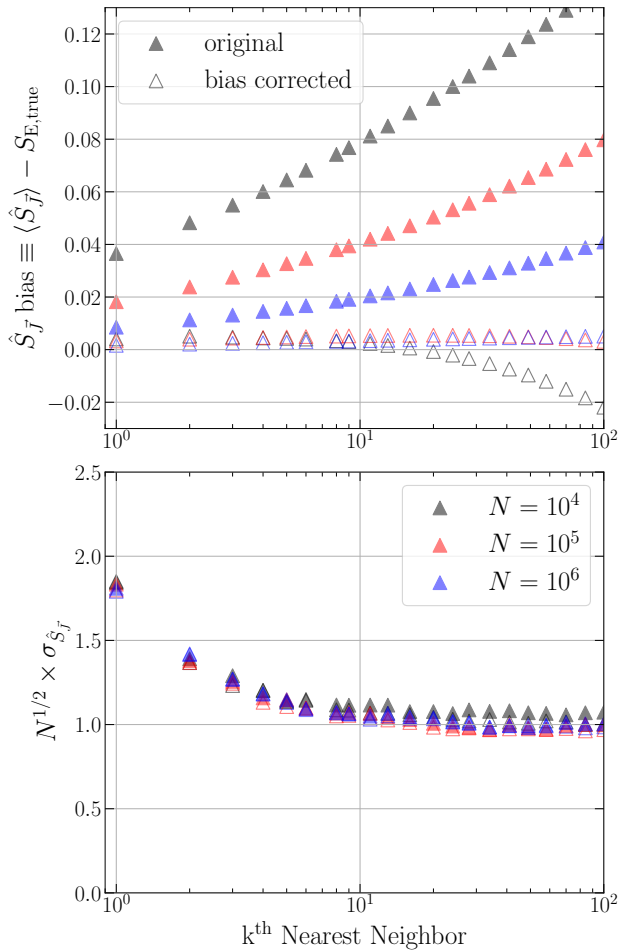


Figure 5. Bias (top) and fluctuation (bottom) of entropy estimates for self-consistent samples of the Isochrone model. We see that the uncorrected bias (full triangles) increases with k , with the correction suppressing the bias. Empty blue and red triangles nearly overlap. The fluctuation $\sigma_{\hat{S}_{\mathcal{J}}}$ decreases with k , saturating at $\sigma_{\hat{S}_{\mathcal{J}}} \approx 1/\sqrt{N}$ for $k \approx 10$.

Fig. 5 (top) shows the corrected biases (empty triangles), which are smaller than the original ones by factors 5 – 15 – note that the empty blue and red triangles nearly overlap. The improvement is even better for larger k , where the bias is not larger than that of $k = 1$ (up to some k , beyond which the bias is over-corrected).

4.4. Entropy fluctuation

As mentioned in Sec. 2, the noise in the entropy estimates is one reason why $\ln \lambda$, Eq. (5), is not a log-likelihood. On theoretical grounds this noise is expected to have amplitude $\sigma_{\hat{S}} \approx N^{-1/2}$ (Biau & Devroye 2015).

Fig. 5 (bottom panel) shows the entropy fluctuations $\sigma_{\hat{S}_{\mathcal{J}}}$, estimated as half the 16–84th-interpercentile range of the realizations, and multiplied by $N^{1/2}$. We confirm the trend that $\sigma_{\hat{S}} \approx N^{-1/2}$, and we see that $\sigma_{\hat{S}}$ decreases

with k , but it saturates at $k \approx 10$, reducing $\sigma_{\hat{S}_{\mathcal{J}}}$ by a factor ≈ 2 in comparison to $k = 1$. Empty triangles show $\sigma_{\hat{S}_{\mathcal{J}}}$ for the bias-corrected estimates, which are nearly identical to those of the uncorrected estimates.

In summary, we conclude that taking $k = 10$ suppresses the noise by a factor 2, and the correction proposed by Charzyńska & Gambin (2015) suppresses the bias without increasing the noise.

5. MINIMUM ENTROPY ILLUSTRATED

In Appendix A, we rigorously demonstrate why the entropy of a fixed sample is minimum in the correct potential, i.e. in the one where the sample is phase-mixed. In this section, we illustrate this with phase-mixed samples in a self-consistent Isochrone model and in potentials of the hypervirial family (Evans & An 2005).

We generate an initial sample of the Isochrone model with $M = b = 1$, and sample size $N/0.7$, selecting the 70% most bound particles in the self-consistent potential, with a final sample of $N \approx 10^4$. This allows us to explore a larger set of models, since we restrict to models where all particles are bound. Note that this cut does not affect the method because the DF is still a function of integrals of motion only, and self-consistency is not required as we explicitly demonstrate below.

We calculate $\hat{S}_{\mathcal{J}}$, i.e. the entropy the sample would have after phase-mixing, on a grid of potentials (M, b), but in this exercise we do not correct the bias discussed in Sec. 4.3. Fig. 6 shows $\hat{S}_{\mathcal{J}}$ values in the grid (M, b), using the nearest neighbor, $k = 1$ (left), and $k = 10$ (right). The magenta dots show the true parameters, and the white X's show the location of the minimum entropy. The white curves are illustrative contours of the 1st, 5-th and 10-th percentiles of $\hat{S}_{\mathcal{J}}$ (not confidence levels). The minimum entropy is indeed very near the true values. We note, however, that its exact location depends on the sample realization. The wrinkles in the colors and contours in the left panel reveal the noise in $\hat{S}_{\mathcal{J}}$ for $k = 1$, while for $k = 10$ the surface is much smoother, in agreement with Fig. 5 (bottom panel).

At this point, the reader might think that the correct identification of the potential with the minimum entropy depends on something special about the Isochrone potential, or on having a self-consistent sample, as opposed to a generic stationary sample. To dispel this concern, we now use the same sample used before as initial conditions and integrate orbits in four different potentials of the hypervirial family (Evans & An 2005) characterized by the potential/density pair

$$\phi(r) = -\frac{GM}{a} \frac{1}{[1 + (r/a)^p]^{1/p}}, \quad (37)$$

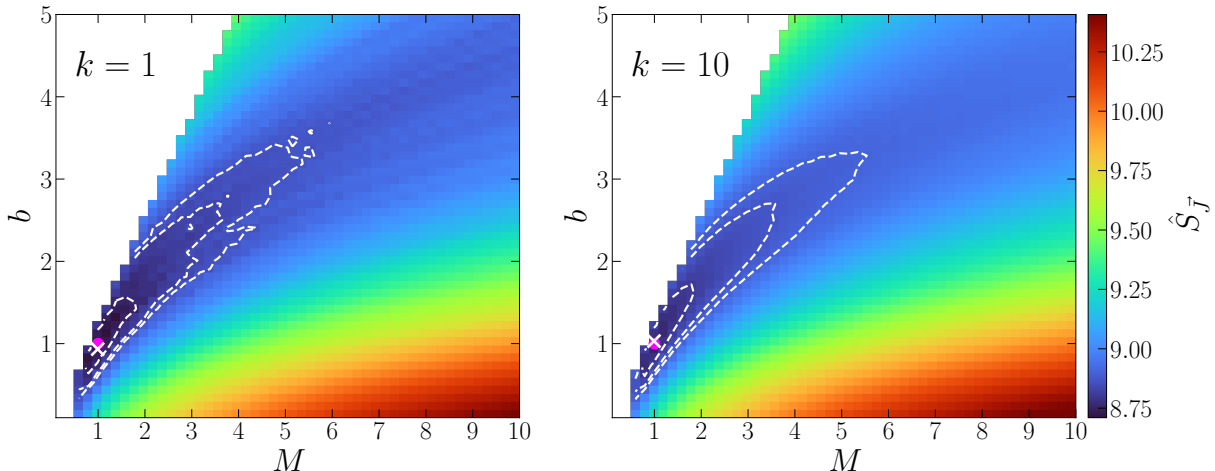
Isochrone potential: $N \approx 10^4$ 

Figure 6. The $\hat{S}_{\vec{J}}$ -surface of a self-consistent sample of the Isochrone model $(M, b) = (1, 1)$ (magenta dots) with actions evaluated on a grid of parameters (M, b) of the Isochrone potential. Contours are percentile levels relative to the minima of $\hat{S}_{\vec{J}}$ (white X's). $\hat{S}_{\vec{J}}$ is estimated with the nearest-neighbor, $k = 1$ (left), and with $k = 10$ (right). As expected from the discussion in Sec. 4.4, a larger k smooths out the $\hat{S}_{\vec{J}}$ -surface. $\hat{S}_{\vec{J}}$ is minimum near the true potential where the sample is phase-mixed.

$$\rho(r) = \frac{(p+1)M}{4\pi a^3} \frac{(r/a)^{p-2}}{[1 + (r/a)^p]^{2+1/p}}, \quad (38)$$

where $0 < p \leq 2$ for the most physically interesting cases. These models have $\rho \sim r^{p-2}$ near the center and $\rho \sim r^{-(p+3)}$ in the outskirts, and have finite mass M . Their most interesting property is that they respect the virial theorem locally, besides the usual global one. We use these models for their simplicity and because they reduce to well known models for $p = 1$ (Hernquist 1990), and $p = 2$ (Plummer 1911). We also explore the cases $p = 1/2$ (strong cusp) and $p = 3/2$ (weak cusp). We set $G = a = 1$, but set $M = 2$ in order to have only bound orbits in all models. We integrate orbits for $100 \times \langle T_{\text{circ}} \rangle$, which is enough for the samples to phase-mix within each of these four potentials. This creates, for each potential, a different equilibrium (phase-mixed) DF, with no explicit analytic expression. Then, for each of these four phase-mixed samples, we calculate the actions $(J_r, J_\varphi, J_\theta)$ and $\hat{S}_{\vec{J}}$ in trial potentials (M, a) , with the corresponding parameter p fixed.

Fig. 7 shows the entropy for these potentials. We see that the minima (white crosses) lie near the true values (magenta dots), but once more their exact locations depend on the particular data realization. This shows that the only requirement to fit the potential by minimizing the entropy is that the sample is phase-mixed, with self-consistency playing no special role. Let us emphasize that this procedure does not require knowledge of the sample's density or anisotropy profile, or its DF,

but only assumes that the DF is an unknown function satisfying the Jeans theorem, i.e. $f = f(\vec{J})$.

Fig. 8 shows a similar picture, but with the entropy calculated in the space of energy and angular momentum, using Eqs. (23)-(25), with T_r calculated as $2\pi/\Omega_r$, where Ω_r is the radial frequency calculated with AGAMA. Once more the entropy minima are close to the true values for all models. We also note that this \hat{S}_{EL} is slightly noisier than $\hat{S}_{\vec{J}}$, even though the former is defined in 2D and its statistical noise is thus expected to be smaller. We suspect that this extra noise in \hat{S}_{EL} may be due to the numerical calculation of the radial period in the density of states, Eqs. (23)-(24), further illustrating the advantages of actions.

6. MODEL FITTING

Having shown that $\hat{S}_{\vec{J}}$ is minimum at the true parameters of the probed potentials, we now perform actual fits to recover the potential where the tracers are in equilibrium. In Sec. 6.1 we fit the Isochrone potential, and in Sec. 6.2 we fit an axisymmetric flattened potential.

6.1. Fitting the Isochrone potential

In order to suppress the noise in the entropy estimates, we generate 100 realizations of a self-consistent sample of the Isochrone Model with $M = b = 1$, and sample size $N/0.7$, selecting the 70% most bound particles in each sample, with final samples of $N \approx 10^4$. Assuming that the final DF (if orbits were integrated until phase-mixing) in each trial Isochrone potential is an unknown function $f(\vec{J})$, we estimate $S_{\vec{J}}$, Eq. (28), for each real-

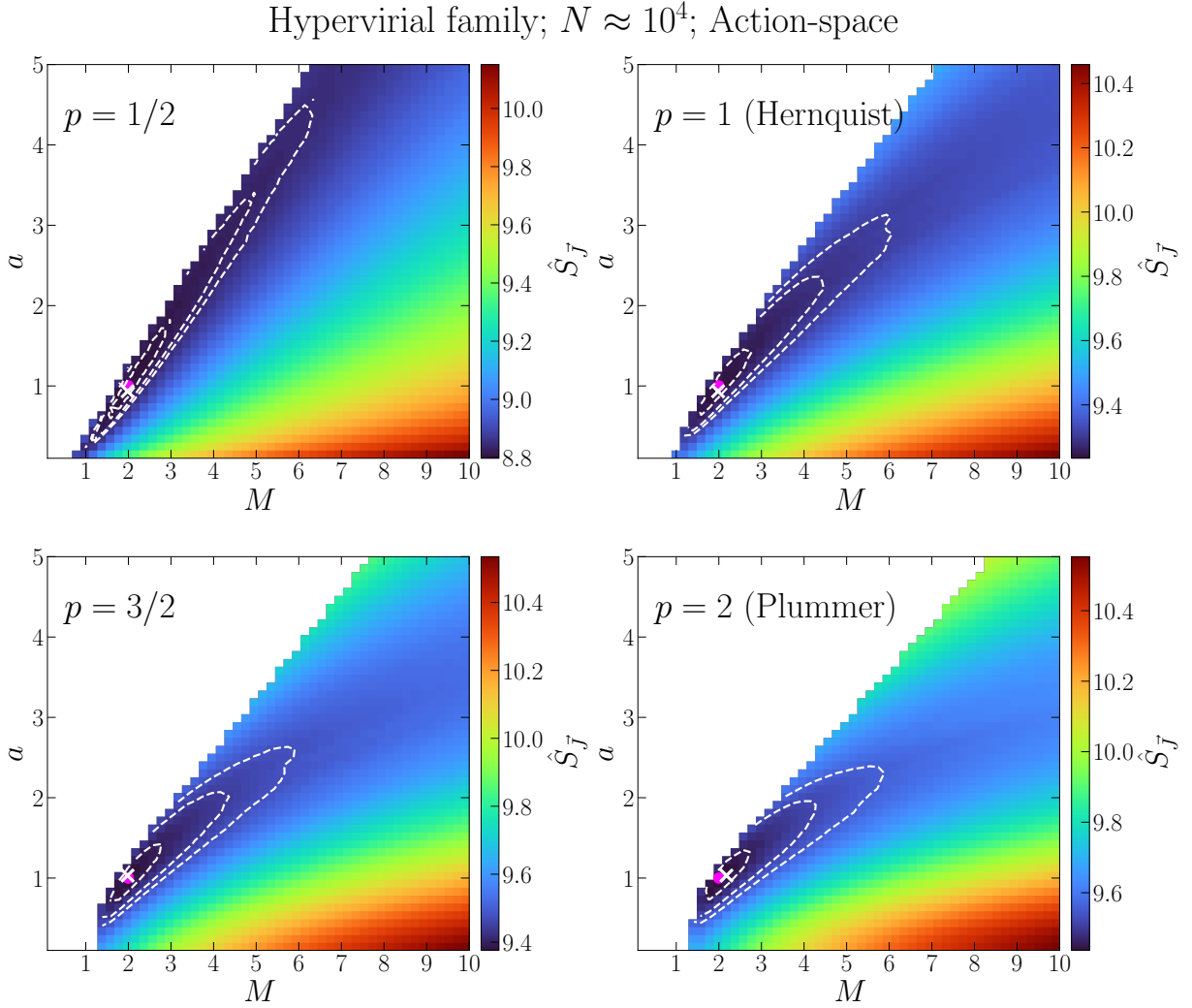


Figure 7. The $\hat{S}_{\mathcal{J}}$ -surface with actions calculated on a grid of parameters (M, a). Each panel is for a different potential of the hypervirial family of Evans & An (2005), where the same initial sample phase-mixed. Magenta dots show the true values, with contours showing percentile levels relative to the minimum of $\hat{S}_{\mathcal{J}}$ (white X). The entropy is estimated with the $k = 10$ nearest-neighbor. For all models, $\hat{S}_{\mathcal{J}}$ has its minimum near the correct parameters.

ization, taking the k -th neighbor with $k = 10$ and correcting for the bias as discussed in Sec. 4.4. We finally calculate the mean over realizations $\langle \hat{S}_{\mathcal{J}} \rangle$.

We use the downhill simplex (“Nelder-Mead”), as implemented in *scipy*, to minimize the mean entropy $\langle \hat{S}_{\mathcal{J}} \rangle$. To prevent trapping at local minima, we fit the data starting with initial parameters in a regular grid of 10×10 points, with $0.1 < M < 10$, and $0.1 < b < 5$. We only fit models with no unbound particle on more than 50% of the realizations and taking the entropy average over those realizations, setting $\langle \hat{S}_{\mathcal{J}} \rangle = \infty$ for the remaining models. We select the best fit model f_0 as the one with smallest $\langle \hat{S}_{\mathcal{J}} \rangle$ among all fits.

Having found the best fit model, we characterize the model’s posterior probability distribution to determine uncertainties and correlations of the parameters. Since we do not have a *bona fide* log-likelihood, we cannot use traditional Markov Chain Monte Carlo sampling. Instead, we use simulation-based inference to characterize the posterior (see Cranmer et al. 2020, for a review). In particular, we perform an Approximate Bayesian Computation (ABC – see Beaumont et al. 2002; Sisson et al. 2018; Martin et al. 2021), a sampling-rejection method that allows sampling the posterior in problems where the log-likelihood is unknown or intractable (see Hahn et al. 2017, for an application in cosmology).

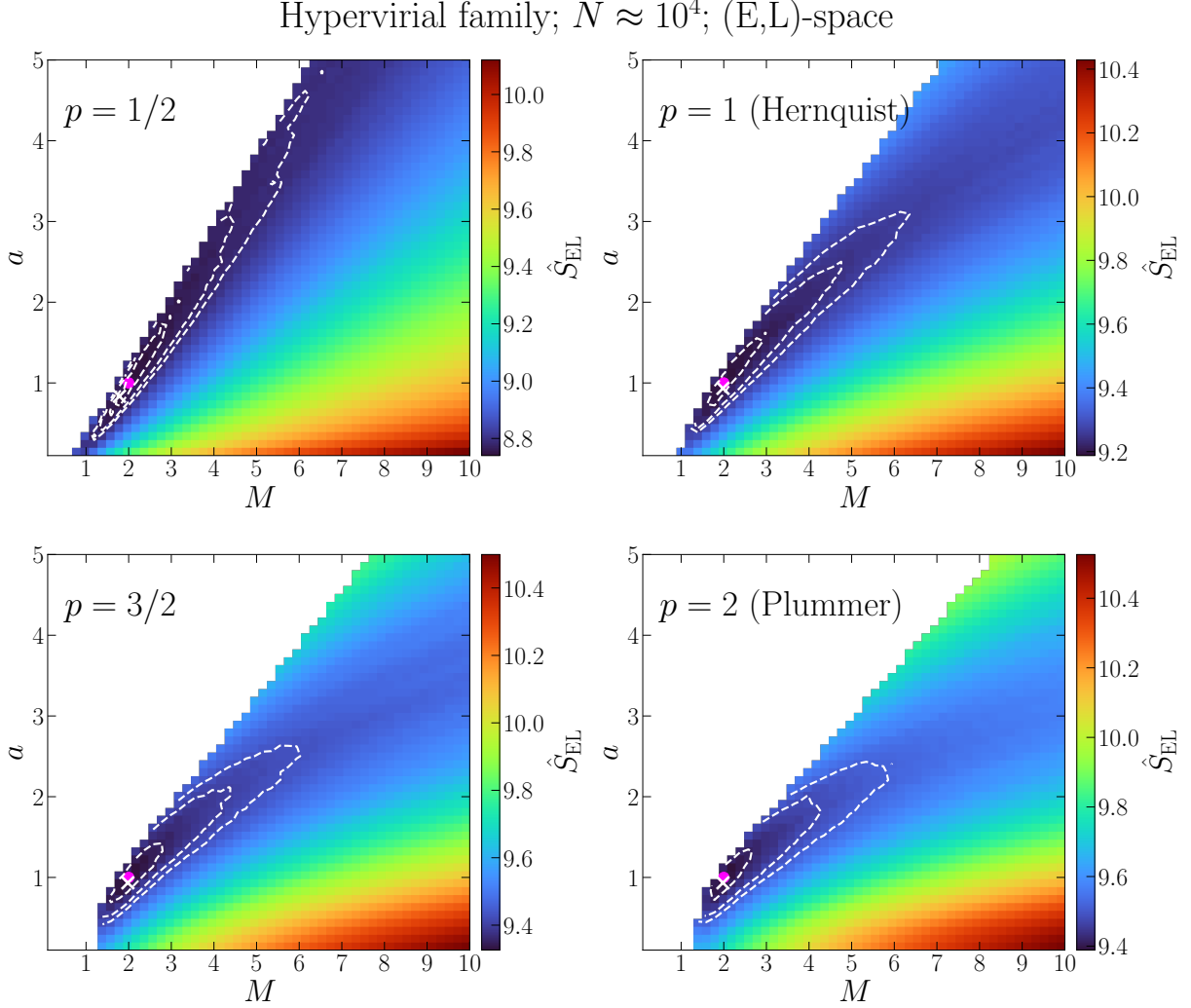


Figure 8. Similar to Fig. 7, but calculated in the (E,L)-space. The minima of $\hat{S}_{E,L}$ (white X) again are close to the true values (magenta dots), but the $\hat{S}_{E,L}$ -surface has more wrinkles, revealing a slightly larger noise.

In an ABC analysis, one starts sampling models from a prior. For each model, a new dataset is generated (simulated) and compared with the observed data via direct comparison or a summary statistic. In our case, the “observed data” are the actions evaluated in the best fit model. The trial model is accepted if the distance between the two datasets is smaller than a threshold ϵ , and rejected otherwise. Depending on the required precision on the posterior, i.e. depending on ϵ , the original method can be very inefficient, and there are different techniques to adapt the sampling function and ϵ iteratively. In this work, we use the sequential Monte Carlo (Sisson et al. 2007) implemented in the Python package pyABC (Schälte et al. 2022). In this algorithm, we first sample from the prior, and subsequently sample from functions that are better approximations of the poste-

rior at each iteration. This is driven by an iterative decrease in ϵ , with a consequent decrease in the samples acceptance rate. The process is considered to converge after ϵ or the acceptance rate fall below a certain value, or the changes in the posterior become negligible.

As a distance metrics between the best fit model f_0 and each trial model f , we use the Kullback-Leibler divergence (see e.g. Jiang 2018)

$$D_{\text{KL}}(f_0||f) \equiv \int f_0 \ln \left(\frac{f_0}{f} \right) d\vec{J} = H(f_0, f) - S_0, \quad (39)$$

where $S_0 = S_{\mathcal{J}}(f_0)$. For two distributions f and g in general, $D_{\text{KL}}(f||g)$ can be seen as a directed distance from f to g . In fact, $D_{\text{KL}}(f||f) = 0$, and it can be shown that $D_{\text{KL}}(f||g) \geq 0$ (Kullback 1968). In practice, we

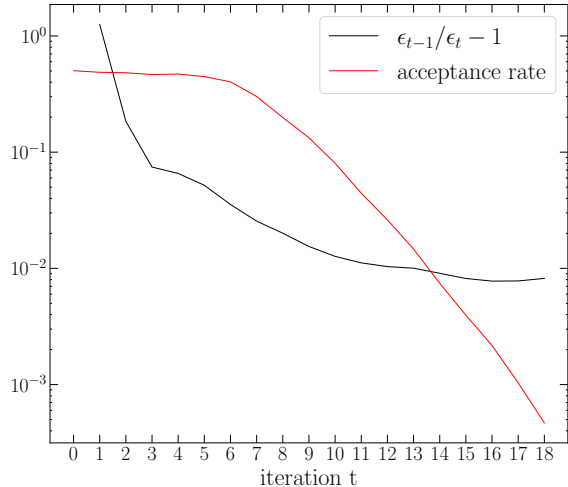


Figure 9. The evolution of the distance threshold ϵ_t and acceptance ratio as a function of the iteration t in the ABC analysis to fit the isochrone potential. In the fit, we estimate $S_{\vec{J}}$, Eq. (27), with the $k = 10$ neighbor.

compute $D_{\text{KL}}(f_0||f)$ using the estimator for the cross-entropy $H(f_0, f)$ – see Eqs. (14)-(16).

We assume flat priors $0.1 \leq M \leq 5$ and $0.1 \leq b \leq 5$ and iterate pyABC until the acceptance rate falls below 10^{-3} , requiring 10^4 models to be accepted in each iteration. Thus, the final iterations are more time consuming since many models are generated until the desired number of models are accepted. ABC requires generating a new data sample for each trial model, otherwise the algorithm converges to point-wise estimates and do not explore the posterior. In order to investigate the ideal situation without observational errors, for each model we generate a different realization of a sample in equilibrium in the best fit model. In practice, when one has a single observed dataset at hand, one can generate new realizations sampling from an assumed error distribution around the observed values, as we do in Sec. 6.2.

Fig. 9 shows the distance threshold ϵ_t and the acceptance rate at each iteration t . After ~ 10 iterations, the distance threshold evolves mildly, while the acceptance rate keeps decreasing steadily, making the sampling inefficient at higher iterations. Fig. 10 shows the approximated posterior at different iterations, with magenta dots showing the true values. It is clear that the algorithm approximately converges after ~ 10 iterations.

Fig. 11 is a corner plot of the last iteration, with blue lines indicating true values, and red contours representing percentiles 39.3 and 86.4 ($1\text{-}\sigma$ and $2\text{-}\sigma$ equivalent contours in 2D). Dashed lines show the percentiles 16, 50 and 84, illustrating the best fit values and $1\text{-}\sigma$ equivalent regions in the marginal distributions of individual

parameters. The true parameters are recovered with $\sim 2\%$ errors, and statistical uncertainties $\sim 10 - 15\%$.

To illustrate the role of the k -th neighbor in the entropy estimate, Fig. 12 shows a corner plot similar to Fig. 11, but now taking $k = 1$, i.e. the nearest neighbor. In agreement with the analysis of Sec. 4.4, in this case the estimates are noisier, resulting in fits that are less accurate, less precise and having less smooth contours, but the true values are still approximately recovered.

6.2. Fitting an axisymmetric potential

We now use a halo-like sample to fit an axisymmetric modified version of the DM halo potential of McMillan (2017), where we introduce a flattening parameter q , i.e. the ratio between the minor and major axes. The potential is that associated with the density profile

$$\frac{\rho_{DM}(\tilde{r})}{\rho_0} = \left(\frac{\tilde{r}}{r_s}\right)^{-\gamma} \left[1 + \left(\frac{\tilde{r}}{r_s}\right)\right]^{\gamma-3} \exp\left[-\left(\frac{\tilde{r}}{400\text{kpc}}\right)^6\right], \quad (40)$$

where $\rho_0 = 8.53702 \times 10^6 M_{\odot}/\text{kpc}^3$, $r_s = 19.5725$ kpc, $\gamma = 1$, $\tilde{r} = \sqrt{x^2 + y^2 + (z/q)^2}$ and $q = 0.7$. The exponential term is just a cutoff to assure a finite mass and to avoid numerical problems. In principle, this DM halo potential could be added to all the other components of the McMillan (2017) potential (such as the thin and thick discs), even if we only fit the parameters of the former. However, in this case the inner potential would be dominated by the baryonic components and the number of star-particles of our tracer sample (described below) in the outer regions would not be large enough to constrain the DM halo parameters. Therefore in what follows we use the DM halo potential only.

We use AGAMA to generate a spherical stellar halo sample of $N = 10^4$ particles (the tracers), with a broken power-law density profile given by

$$\rho_h(r) \propto \left(\frac{r}{r_h}\right)^{-2.5} \left[1 + \left(\frac{r}{r_h}\right)\right]^{-0.5} \exp\left[-\left(\frac{r}{300\text{kpc}}\right)^3\right], \quad (41)$$

where $r_h = 25$ kpc, and the exponential term is again a cutoff at large radii to avoid numerical problems. We set the velocities such that this sample is stationary in our axisymmetric potential. Specifically, we first create a sphericalized version of the potential and initialize the isotropic DF using the Eddington inversion formula, then express this DF as a function of actions, embed it in the flattened potential, and sample positions and velocities of stars from the resulting system. This procedure is equivalent to adiabatically deforming the potential from the initial (spherical) to the final (non-spherical) shape.

With this sample, assumed to be described by an unknown DF $f(\vec{J})$, we fit the potential parameters ρ_0 , q , γ ,

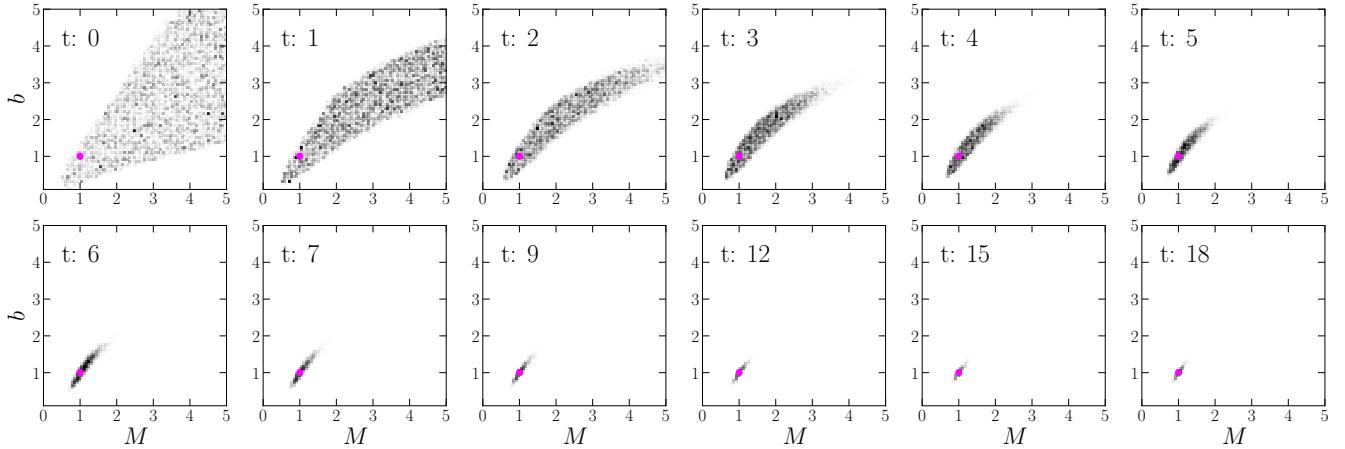


Figure 10. The evolution of the approximated posterior distribution as a function of the iteration t in the ABC analysis to fit the isochrone potential. The true parameters $(M, b) = (1, 1)$ are indicated by magenta dots. We estimate $S_{\vec{J}}$, Eq. (27), with the $k = 10$ neighbor, and correct for the bias as discussed in Sec. 4.3.

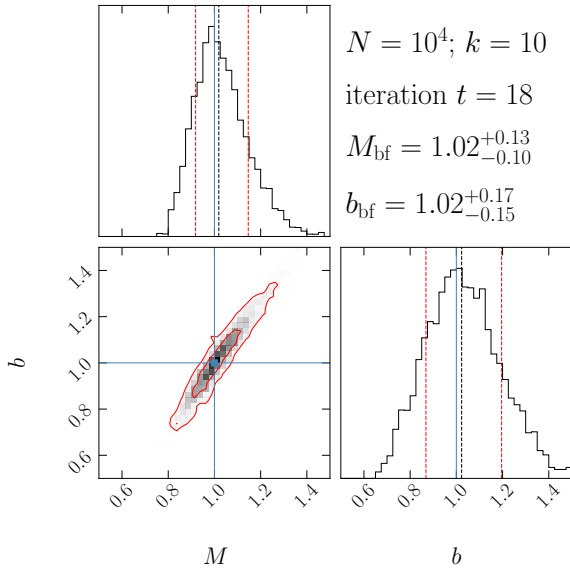


Figure 11. The final posterior on the parameters of the isochrone potential, and respective histograms. This is obtained for a phase-mixed sample of $N \approx 10^4$ particles in an isochrone potential ($M = 1, b = 1$).

and r_s . We estimate the actions $\vec{J} = (J_r, J_\varphi, J_z)$ in each trial potential through the Stackel fudge (Binney 2012) using AGAMA. As in Sec. 6.1, we first identify the best fit model minimizing $\langle \hat{S}_{\vec{J}} \rangle$, Eq. (28), starting in a grid of parameter values, and averaging the entropy estimates over 100 sample realizations. We then use the actions in the globally best fit model as the “observed data” in the ABC to characterize the parameters’ posterior.

Once more, we run pyABC accepting 10^4 models in each iteration, generating a new size- N data sample for each potential. Unlike Sec. 6.1, where each new sam-

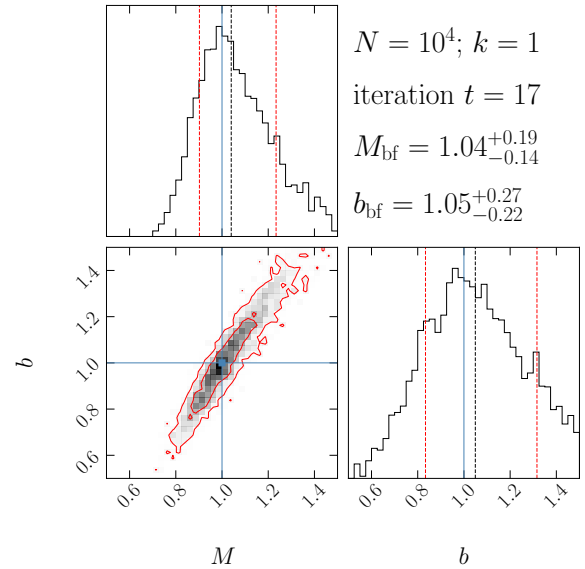


Figure 12. Similar to Fig. 11, but taking the $k = 1$ nearest neighbor in the entropy estimate.

ple was an equilibrium sample of the best fit model, here we sample from a Gaussian error distribution centered on the “observed coordinates”, as one would do when dealing with observational data, and correlated uncertainties can be easily introduced with a covariance matrix. Fig. 13 shows the corner plot obtained for 1% uncertainty on all phase-space coordinates (Gaussians of width $\sigma_{w_i}/|w_i| = 0.01$). We run pyABC until the acceptance rate falls below 10^{-2} , by which time the true parameters are well recovered. This suggests that this is a reasonable choice when dealing with observed data, where the true answer is unknown.

Fig. 14 shows a similar plot, obtained with Gaussian error distributions with $\sigma_{w_i}/|w_i| = 0.2$ for each coordinate, which is more realistic and maybe a little pessimistic. We clearly see the worsening of the fit compared to Fig. 13, but the true parameters are still recovered reasonably well. In particular, the flattening parameter is recovered with uncertainty $\sim 10\%$.

7. DISCUSSION

7.1. Time evolution versus fixed sample

In Sec. 3, we introduced expressions for the entropy of DFs that are functions of integrals of motion. On the one hand, one can think of Eqs. (17), (21) and (27) as the entropy the system would achieve if the same sample is allowed to evolve in each trial potential until it phase-mixes, with the original DF evolving to another DF that depends only on integrals evaluated in that trial potential. In this case, minimizing Eq. (17), (21) or (27) corresponds to minimizing the future entropy, for the sample will phase-mix if put in a wrong potential, increasing the entropy. Interestingly, we do not need to wait for the time evolution, since integrals are conserved and can therefore be evaluated at the onset in each potential. The DF evolution is purely driven by the remaining variables (e.g. angles), which evolve to a uniform distribution in their respective supports.

On the other hand, in Appendix A we demonstrate that, for a fixed equilibrium sample of a DF $f(\vec{r}, \vec{v})$,

$$S_Y \geq S(f), \quad (42)$$

where $S(f)$ is the sample's invariant entropy and

$$S_Y = - \int F(\vec{y}) \ln \left[\frac{F(\vec{y})}{g(\vec{y})} \right] d^m \vec{y} \quad (43)$$

is the general form of Eqs. (17), (21) and (27), with \vec{y} being a set of m integrals and $g(\vec{y})$ the density of states. In this case, with no time evolution implied, the marginalization defining the integrals' pdf $F(\vec{y})$, Eq. (A3), is considered even when the remaining variables are not uniformly distributed, i.e. when the sample is not stationary. In Appendix A we show that in the correct potential, where the remaining variables are uniformly distributed in their supports, $S_Y = S(f)$.

These two different interpretations require minimizing the same quantity S_Y , showing that they are completely equivalent. Thus, for potentials where stationary states are synonymous with uniform distributions in the remaining variables (not true in exceptional cases such as the harmonic oscillator), the rigorous derivation of Eq. (42) – see Appendix A – can be seen as a demonstration of the second law of thermodynamics for collisionless gravitational systems in these potentials, i.e.

of the inevitability of the entropy increase for a sample starting out of equilibrium, as illustrated in Fig. 3.

7.2. Why does the method work?

It is commonly accepted that the evolution of a collisionless system, i.e. one in a smooth potential ϕ , is necessarily described by the Vlasov (or Collisionless Boltzmann) equation

$$\frac{df}{dt} \equiv \frac{\partial f}{\partial t} + \vec{v} \cdot \frac{\partial f}{\partial \vec{r}} - \frac{\partial \phi}{\partial \vec{r}} \cdot \frac{\partial f}{\partial \vec{v}} = 0, \quad (44)$$

which assumes $N \rightarrow \infty$ and implies entropy conservation. If that was the case, the success of the minimum-entropy method for fitting potentials demonstrated in this work would be rather surprising.

In Sec. 4, we explored self-consistent samples of the Isochrone model with mass $M = 1$, which has analytical expressions for $f(E)$, $g(E)$ and actions. This allows us to calculate the true entropy to machine precision, and compare it with estimates in 6D, and using integrals of motion, i.e. assuming $f = f(E)$, $f = f(E, L)$ or $f = f(\vec{J})$, which are all valid assumptions in this case. In particular, we get a relative error $\delta S_{\text{EL}}/S_{\text{E,true}} \lesssim 0.01\%$ for $N = 10^8$ in the (E, L) -space.

We then evolved this sample in a different Isochrone potential with mass $M = 3$, and followed the entropy evolution for size- N samples. From the Jeans theorem, the final DF must be a function $f = f(E, L)$. This $f(E, L)$ is unknown, and the final entropy cannot be calculated with simple integration, but is estimated with \hat{S}_{EL} with the same expected small error for $N = 10^8$.

Thus, knowing its initial and final values, we conclude that the entropy must increase for the sample to achieve a phase-mixed state described by Jeans theorem – see Fig. 3. This seems intuitive and in agreement with the second law of thermodynamics, but it contrasts with the entropy conservation predicted by Eq. (44). This wrong prediction follows from the limit $N \rightarrow \infty$ assumed by this equation, implying the development of indefinitely fine phase-space structures, i.e. indefinitely large wave numbers k in Fourier space. Fortunately, real gravitational samples are finite- N and, because of this, evolve to stationary states constrained by Jeans theorem.

It is normally assumed that Eq. (44) is only invalidated on timescales comparable to the collisional relaxation time, $\tau_{\text{col}} \propto (N/\ln N) \tau_{\text{cr}}$, where τ_{cr} is the crossing time. Note that if N is large enough to suppress the collisional relaxation (i.e. for the potential to be smooth), one can only extrapolate to $N \rightarrow \infty$ under the assumption that there is no other (collisionless) relaxation time scale with weaker N -dependence. Such a collisionless relaxation timescale does exist, and it is given

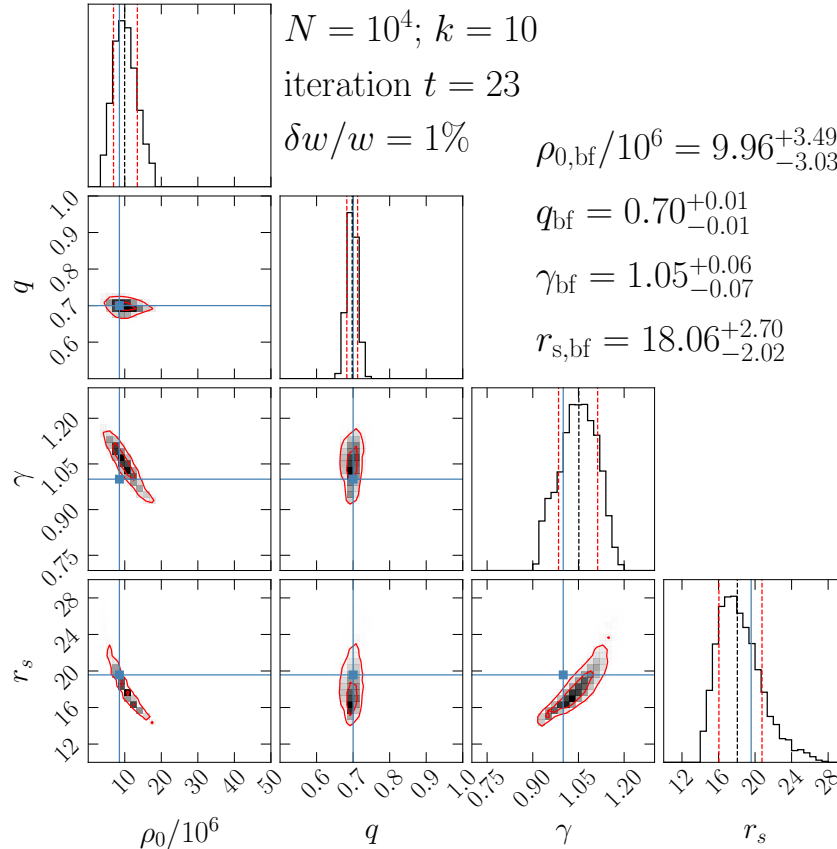


Figure 13. pyABC results for $N = 10^4$ particles that phase-mixed in a flattened axisymmetric potential ($q = 0.7$). Each of the 6D coordinates is assumed to have a Gaussian error distribution with relative uncertainties $\delta w/w = 0.01$. The true parameters (blue lines/dots) are well recovered, except for a small bias in the space of r_s vs γ , which requires further investigation.

by $\tau \lesssim 0.1N^{1/6}\tau_{\text{cr}}$ (Beraldo e Silva et al. 2019b), i.e. a few τ_{cr} even for samples as large as a galaxy ($N \sim 10^{11}$).

This collisionless relaxation has its roots in the Nyquist-Shannon theorem (Nyquist 1928; Shannon 1949): in d -dimensions, a size- N sample can only represent functions with maximum wave number $k \lesssim N^{1/d}$. Functions with higher wave numbers (sharper features) introduce information not contained in the sample. As shown by Beraldo e Silva et al. (2019a), this theorem constrains the finest structures allowed for a DF describing a real, i.e. finite- N , system. The maximum wave number increases linearly with time for integrable systems, and faster for non-integrable ones, until hitting the Nyquist-Shannon upper limit. After that, the system approaches a steady state constrained by the Jeans theorem, and *does not produce the extra fine phase-space structures predicted by Eq. (44)* – for recent discussions around this point in plasma physics, see Zhdankin (2022, 2023); Ewart et al. (2023); Nastac et al. (2024).

This contrasts with the traditional view that the underlying evolution of collisionless systems is governed by Eq. (44), while the entropy increase is due to informa-

tion loss in the measurement process, i.e. some sort of coarse-graining (e.g. Lynden-Bell 1967; Tremaine et al. 1986; Dehnen 2005; Levin et al. 2014; Barbieri et al. 2022; Banik et al. 2022). Although the work of Dehnen (2005) is the closest to our interpretation, it still assumes that the underlying evolution is described by Eq. (44), and that the evolution to a stationary state requires coarse-graining. Besides the reasons given above, the effectiveness of the method presented here and the excellent agreement of the entropy estimates for DFs depending on different integrals of motion (see Figs.2-3) shows that that is not the case. After all, agreement of estimates in different spaces would require, if based on coarse-graining, careful choice of the coarse-grain scales, which is not required in our approach.

We conclude that the method works because it explores an objective entropy increase associated with the phase-mixing of real, i.e. finite- N , collisionless systems.

7.3. Future improvements

An ideal method to constrain a gravitational potential using the kinematics of a stellar sample should:

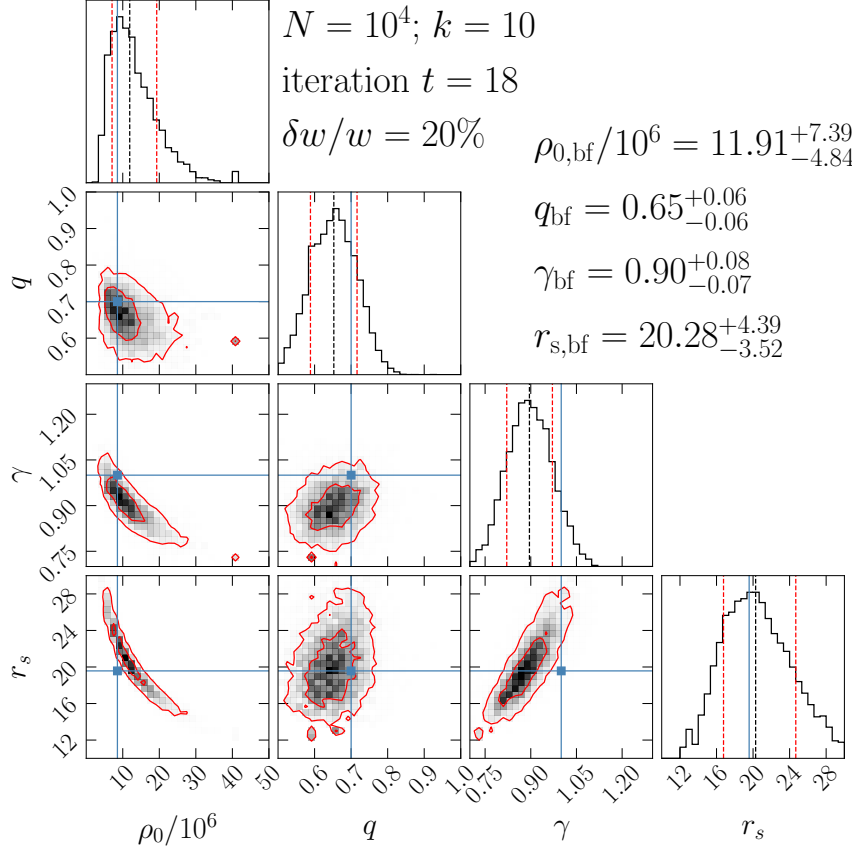


Figure 14. Similar to Fig. 13, but now assuming each coordinate to have Gaussian uncertainties $\delta w/w = 0.2$. We see the worsening of the fit, but the true parameters are still overall well recovered.

1. allow constraints on general mass distributions, including general axisymmetric and triaxial systems;
2. properly incorporate uncertainties and covariances in the data, providing not only best fit values, but full probability distributions of the fit parameters;
3. avoid making any assumptions regarding the DF besides the requirements of the Jeans theorem;
4. be computationally efficient in order to handle samples with $\sim 10^4 - 10^6$ stars, typical of stellar halo samples, or stars within a globular cluster;
5. properly consider the survey's footprint and selection function;
6. handle incomplete information, e.g. samples missing line-of-sight velocities and/or distances.

We demonstrated that our method already satisfies items 1–4. Although we have not tested it for triaxial potentials, the only difficulty is to efficiently estimate actions in such potentials. With these actions at hand one can also investigate triaxial systems with this method.

In Sec. 4, we discussed the bias and noise associated with the k NN entropy estimator used in this paper. Although this estimator is good enough for most applications, our method would benefit from more precise and accurate estimates. In the future, it will be important to explore more recent techniques aimed to improve on these estimates – see e.g. Lombardi & Pant (2016); Berrett et al. (2019); Ao & Li (2023) for recent works.

In Sec. 4.3, we showed that the bias correction proposed by Charzyńska & Gambin (2015) effectively suppressed the bias in the entropy estimates for self-consistent samples of the Isochrone model. This correction assumes the sample's support is a parallelepiped defined by the extreme values of each coordinate. The typical action-space of a self-consistent sample of an axisymmetric potential has a shape close to a tetrahedron with two perpendicular faces (see Fig. 3.25 in Binney & Tremaine 2008). The reason why this simple correction worked so well in the self-consistent Isochrone sample is probably that this tetrahedron support is not so different from the assumed parallelepiped support for most stars. For non self-consistent samples, and particularly for samples with sharp geometric cuts, the actual sup-

port in action-space can be more complicated. For these cases, it will be important to implement bias corrections that apply to samples with support of a general shape.

In the DF-fitting method, where one assumes an analytical expression for the DF, selection effects due to geometric cuts are taken into account by the normalization factor $A = \int_{\mathcal{V}} f(\vec{w}|\vec{p})\mathcal{S}(\vec{w}) d^6\vec{w}$, where \mathcal{V} is the survey volume. This integral can be very complicated and time consuming, and its limited numerical accuracy is the main source of noise in these methods (McMillan & Binney 2013; Hattori et al. 2021). In the minimum-entropy method developed in this paper, we do not have an analytic DF, but the survey footprint can be accounted by the fractional time each orbit spends in it – see Eq. (A10). This can be done either by generating a number of angle variables uniformly distributed in $[0, 2\pi)$ for each star and checking how many pairs $(\vec{\theta}, \vec{J})$ end up inside the footprint, or simply integrating orbits and directly counting the fractional time inside the footprint for each orbit.

Other important improvements involve handling unbound stars, such as hyper-velocity stars, and samples with missing data.

7.4. Comparison with other methods

The orbital pdf method developed by Han et al. (2016) and its successor emPDF (Li et al. 2024) propose recovering the underlying potential exploring the Jeans theorem but without specifying a DF, in a similar vein as the minimum-entropy method developed here. Their methods are currently restricted to spherical systems, but can be extended into action space in a more general geometry. Their underlying general principles and final expressions are similar to those we derive for the spherical case, although based on different physical arguments and developed independently. While Li et al. (2024) focus on estimating the DF using Kernel Density Estimates, our approach uses well established recipes to estimate the differential entropy of a sample via k-Nearest Neighbors (but other estimators can be use too).

Thus, in some sense, emPDF and the minimum-entropy method represent two different views of the same general principles. Nonetheless, we believe the general formalism developed in the current work illuminates not only fundamental aspects of any method to constrain mass distributions exploring the Jeans theorem, but also our picture of the evolution of collisionless systems towards stationary states.

7.5. Disequilibrium in the MW

Complicating the application of the minimum-entropy method to the MW is the kinematic perturbation from

the Large Magellanic Cloud (LMC), currently near a pericentric passage (at a distance of ≈ 50 kpc, Besla et al. 2007). This perturbation is significant enough to produce a reflex motion of the MW disc and its inner halo ($\lesssim 30$ kpc) towards the LMC past trajectory (Garavito-Camargo et al. 2021; Petersen & Peñarrubia 2021; Erkal et al. 2021). Thus, dynamical equilibrium cannot be assumed for the outer halo ($\gtrsim 30$ kpc). However, if one wants to probe the outer halo still assuming dynamical equilibrium, a promising avenue is to try to “undo” or correct for the kinematical perturbation from the LMC (Deason et al. 2021; Correa Magnus & Vasiliev 2022). On the other hand, for the inner halo ($\lesssim 30$ kpc) the assumption of equilibrium still seems reasonable.

8. SUMMARY

We have presented a method to constrain the gravitational potential where a tracer sample is in dynamical equilibrium. It is based on the idea that, if put in a different potential, this sample would phase-mix, producing an entropy increase. The potential is then recovered by minimizing the future entropy of the sample with respect to the parameters of the potential. This entropy is estimated using integrals of motion, and the parameters of the potential enter the fit through these integrals.

We focused on actions, and demonstrated their advantages, including possible constraints on the MW’s DM halo shape. Investigation of this particular problem will benefit from large spectroscopic surveys such as the DESI-MWS (Cooper et al. 2023) in tandem with Gaia. The method can be similarly applied to other integrals, such as energy and angular momentum, e.g. in the study of spherical systems like globular clusters – see the demonstration in Appendix A. Finally, in Appendix B we discuss the possibility of recovering a potential by maximizing the samples’ entropy in angle-space, concluding that this is not expected to work in general.

ACKNOWLEDGEMENTS

LBeS thanks Wyn Evans, Josh Speagle, Chirag Modi, David Hogg, Bernardo Modenesi, Sergey Koposov, Zhaozhou Li, Carrie Filion and the stellar halos group at the University of Michigan for useful discussions, and the support provided by the Heising Simons Foundation through the Barbara Pichardo Future Faculty Fellowship from grant # 2022-3927. MV and LBeS acknowledge the support of NASA-ATP award 80NSSC20K0509 and U.S. National Science Foundation AAG grant AST-2009122. EV thanks Hans-Walter Rix and Kathryn Johnston for valuable comments, and acknowledges support from an STFC Ernest Rutherford fellowship (ST/X004066/1). KH is supported by JSPS

KAKENHI Grant Numbers JP24K07101, JP21K13965, and JP21H00053. WdSP is supported by CNPq (309723/2020-5). KJD acknowledges support provided by the Heising Simons Foundation grant # 2022-3927. We respectfully acknowledge that the University of Arizona is on the land and territories of Indigenous peoples. Today, Arizona is home to 22 federally recognized

tribes, with Tucson being home to the O’odham and the Yaqui. We respect and honor the ancestral caretakers of the land, from time immemorial until now, and into the future.

Software: numpy (Harris et al. 2020), scipy (Virtanen et al. 2020), Agama (Vasiliev 2019), pyABC (Schälte et al. 2022).

APPENDIX

A. MATHEMATICAL BASIS OF THE MINIMUM-ENTROPY METHOD

For a DF separable in the space of angles-actions, $f(\vec{\theta}, \vec{J}) = \mathcal{F}(\vec{\theta})F(\vec{J})$, the entropy, Eq. (1), is the sum of the respective sub-spaces’ entropies, $S(f) = S(\mathcal{F}(\vec{\theta})) + S(F(\vec{J}))$. From Jeans theorem, the angle distribution is uniform, $\mathcal{F}(\vec{\theta}) = (2\pi)^{-3}$, and thus $S(\mathcal{F}(\vec{\theta}))$ is maximum, in the potential where the sample is stationary. Since $S(f)$ is invariant for changes of variables, i.e. for angle-actions evaluated in any potential, $S(F(\vec{J}))$ is minimum in that potential.

Here we generalize this idea to non-separable DFs. In fact, one can always separate pdf’s in terms of conditional pdf’s, e.g. $f(\vec{\theta}, \vec{J}) = \mathcal{F}(\vec{\theta}|\vec{J})F(\vec{J})$, where $\mathcal{F}(\vec{\theta}|\vec{J})$ is the conditional pdf of $\vec{\theta}$, given \vec{J} . Thus, loosely speaking, we have $S(f) = S(\mathcal{F}(\vec{\theta}|\vec{J})) + S(F(\vec{J}))$ and can recover the potential by minimizing $S(F(\vec{J}))$, since $S(\mathcal{F}(\vec{\theta}|\vec{J}))$ is maximum at any given action in the right potential. Below we formalize this idea and generalize it to other integrals.

Given the DF $f(\vec{w})$, where $\vec{w} \equiv (\vec{r}, \vec{v})$, consider a random variable $X = (X_1, \dots, X_n)$, with $X_i = X_i(\vec{w})$. Let F_X be the pdf of X , i.e. F_X is a positive and normalized function on \mathbb{R}^n . The expectation value of X is

$$\mathbb{E}[X] = \int_{-\infty}^{\infty} f(\vec{w})X(\vec{w}) \, d^6\vec{w} = \int_{-\infty}^{\infty} F_X(\vec{x})\vec{x} \, d^n\vec{x}. \quad (\text{A1})$$

Let $\vec{y} = (y_1, \dots, y_m)$, with $m < 6$, be a second random variable, with $y_i = y_i(\vec{w})$ – we will later make \vec{y} be the integrals of motion, e.g.: for spherical and isotropic systems, we set $y_1 = E$; for spherical and anisotropic ones, we set $(y_1, y_2) = (E, L)$; for angle-action variables, $(y_1, y_2, y_3) = \vec{J}$. In general, we require \vec{y} to have the following property:

1. There is a smooth function $\Psi : \mathbb{R}^6 \rightarrow \mathbb{R}^6$, whose Jacobian matrix

$$(J_\Psi)_{ij} \doteq \frac{\partial \Psi_i}{\partial w_j}, \quad i, j = 1, \dots, 6$$

is non-degenerate (i.e., its determinant is non-vanishing), such that $y_k(\vec{w}) = \Psi_{6-m+k}(\vec{w})$, $k = 1, \dots, m$. In other words, \vec{y} corresponds to the last $m < 6$ coordinates of some change of variables Ψ in 6D.

For random variables \vec{y} with this property, we consider the conditional expectation in the sense of a “disintegration” of f with respect to \vec{y} , $\mathcal{F}(\cdot|\vec{y})_{\vec{y} \in \mathbb{R}^m}$ – for a friendly, yet thorough, introduction to this topic, see Chang & Pollard (1997). This is a family of pdf’s such that for each \vec{y} , it gives the pdf $\mathcal{F}(\vec{z}|\vec{y})$ of the remaining variables $\vec{z} \in \mathbb{R}^{6-m}$. This pdf is properly normalized and is different from marginalizing over \vec{y} , or from simply taking f at fixed \vec{y} values. Given that the pdf of the new variables (\vec{z}, \vec{y}) is $f(\Psi^{-1}(\vec{z}, \vec{y})) \cdot |J_{\Psi^{-1}}(\vec{z}, \vec{y})|$, and not $f(\Psi^{-1}(\vec{z}, \vec{y}))$ alone, the conditional probability with respect to \vec{y} is explicitly given by:

$$\mathcal{F}(\vec{z}|\vec{y}) = \frac{f(\Psi^{-1}(\vec{z}, \vec{y})) |J_{\Psi^{-1}}(\vec{z}, \vec{y})|}{F(\vec{y})}, \quad (\text{A2})$$

where

$$F(\vec{y}) = \int_{-\infty}^{\infty} f(\Psi^{-1}(\vec{z}', \vec{y})) |J_{\Psi^{-1}}(\vec{z}', \vec{y})| \, d^{6-m}\vec{z}' \quad (\text{A3})$$

is the pdf of the random variable \vec{y} , i.e., the marginalization over the remaining variables \vec{z} . Moreover, as expected, F only depends on \vec{y} , and not on the particular choice of the transformation $\Psi : \mathbb{R}^6 \rightarrow \mathbb{R}^6$ for the remaining variables \vec{z} , since Eq. (A3) marginalizes over them. This elementary remark is important later on in this appendix. Note that if $f = f(\vec{y})$, i.e. if it is uniform in \vec{z} , Eq. (A3) reduces to Eq. (18), (22) or (26) as particular cases.

With the change of variables $\vec{w} \rightarrow (\vec{z}, \vec{y})$ in Eq. (A1) we get:

$$\mathbb{E}[X] = \int_{-\infty}^{\infty} f(\vec{w})X(\vec{w}) d^6\vec{w} = \int_{-\infty}^{\infty} X(\Psi^{-1}(\vec{z}, \vec{y})) f(\Psi^{-1}(\vec{z}, \vec{y})) |J_{\Psi}(\vec{y}, \vec{z})| d^{6-m}\vec{z} d^m\vec{y},$$

and from Eq. (A2) results that

$$\begin{aligned} \mathbb{E}[X] &= \int_{-\infty}^{\infty} X(\Psi^{-1}(\vec{z}, \vec{y})) \mathcal{F}(\vec{z}|\vec{y}) F(\vec{y}) d^{6-m}\vec{z} d^m\vec{y} \\ &= \int_{-\infty}^{\infty} F(\vec{y}) \left(\int_{-\infty}^{\infty} \mathcal{F}(\vec{z}|\vec{y}) X(\Psi^{-1}(\vec{z}, \vec{y})) d^{6-m}\vec{z} \right) d^m\vec{y}. \end{aligned}$$

In fact, the last equality is the formal *definition* of $\mathcal{F}(\cdot|\vec{y})_{\vec{y} \in \mathbb{R}^m}$ being the disintegration of the DF with respect to the random variable \vec{y} . Making $X = -\ln f$ and using Eq. (A2), we get

$$\begin{aligned} S(f) = \mathbb{E}(-\ln f) &= \int_{-\infty}^{\infty} F(\vec{y}) \left\{ \int_{-\infty}^{\infty} \mathcal{F}(\vec{z}|\vec{y}) \cdot [-\ln f(\Psi^{-1}(\vec{z}, \vec{y}))] d^{6-m}\vec{z} \right\} d^m\vec{y} \\ &= \int_{-\infty}^{\infty} F(\vec{y}) \left\{ \int_{-\infty}^{\infty} \mathcal{F}(\vec{z}|\vec{y}) \cdot \left[-\ln \left(\frac{F(\vec{y})}{|J_{\Psi^{-1}}(\vec{y}, \vec{z})|} \mathcal{F}(\vec{z}|\vec{y}) \right) \right] d^{6-m}\vec{z} \right\} d^m\vec{y}. \end{aligned}$$

Writing the logarithm of the product as the sum of logarithms, we get

$$\begin{aligned} S(f) &= \int_{-\infty}^{\infty} F(\vec{y}) \left\{ \int_{-\infty}^{\infty} \mathcal{F}(\vec{z}|\vec{y}) \ln |J_{\Psi^{-1}}(\vec{y}, \vec{z})| d^{6-m}\vec{z} \right\} d^m\vec{y} - \int_{-\infty}^{\infty} F(\vec{y}) \ln F(\vec{y}) d^m\vec{y} \\ &\quad - \int_{-\infty}^{\infty} F(\vec{y}) \left\{ \int_{-\infty}^{\infty} \mathcal{F}(\vec{z}|\vec{y}) \ln \mathcal{F}(\vec{z}|\vec{y}) d^{6-m}\vec{z} \right\} d^m\vec{y}, \end{aligned}$$

where for the second term in the right-hand side we used the fact that $\int_{-\infty}^{\infty} \mathcal{F}(\vec{z}|\vec{y}) d^{6-m}\vec{z} = 1$. Hence,

$$S(f) = \mathbb{E}[\ln |J_{\Psi^{-1}}|] + S(F(\vec{y})) + \mathbb{E}_{\vec{y}}[S(\mathcal{F}(\cdot|\vec{y}))], \quad (\text{A4})$$

where $\mathbb{E}_{\vec{y}}[S(\mathcal{F}(\cdot|\vec{y}))]$ denotes the expectation of the entropy

$$S(\mathcal{F}(\cdot|\vec{y})) \doteq - \int_{-\infty}^{\infty} \mathcal{F}(\vec{z}|\vec{y}) \ln [\mathcal{F}(\vec{z}|\vec{y})] d^{6-m}\vec{z} \quad (\text{A5})$$

of the conditional pdf's. Note that these entropies define a random variable that only depends on \vec{y} . In particular, if Ψ is a canonical transformation ($|J_{\Psi^{-1}}(\vec{y}, \vec{z})| = 1$), from Eq. (A4) we have $S(f) = S(F(\vec{y})) + \mathbb{E}_{\vec{y}}[S(\mathcal{F}(\cdot|\vec{y}))]$.

Eq. (A4) is the main general result of this appendix. We show below that it justifies our minimum-entropy method for fitting galactic potentials. With this aim, it is convenient to make the following additional assumption on the variable transformation Ψ , and afterwards we show how it can be removed:

2. The Jacobian determinant $|J_{\Psi^{-1}}(\vec{y}, \vec{z})|$ only depends on \vec{y} .

In fact, given a partial transformation $\tilde{\Psi} : \mathbb{R}^{6-m} \rightarrow \mathbb{R}^{6-m}$, it is common to find a point transformation for the remaining variables such that the total new transformation $\Psi : \mathbb{R}^6 \rightarrow \mathbb{R}^6$ is even *canonical*, i.e. $|J_{\Psi^{-1}}(\vec{y}, \vec{z})| = 1$.

Suppose that, for all $\vec{y} \in \mathbb{R}^m$, the maximum allowed support of the pdf's $\mathcal{F}(\cdot|\vec{y})$ is some bounded region $\Omega_z(\vec{y})$ of \mathbb{R}^{6-m} . The region $\Omega_z(\vec{y})$ encodes the set of coordinates $\vec{z} \in \mathbb{R}^{6-m}$ corresponding to particles that, at fixed \vec{y} , are *not* forbidden to appear in the sample, e.g. for being unbound or for its coordinates lying outside the survey footprint.

If the coordinates $\vec{y} \in \mathbb{R}^m$ are constants of motion, one expects that the original DF $f(\vec{w})$ is stationary (phase-mixed), or, more generally, a cut of some stationary DF if, and only if, $f(\Psi^{-1}(\vec{z}, \vec{y}))$ is constant for \vec{z} within the maximum allowed support $\Omega_z(\vec{y})$, at any fixed $\vec{y} \in \mathbb{R}^m$. *This refers to Jeans theorem*. Thus, here we tacitly use this property of the DF as equivalent to its stationarity. If condition 2. above is fulfilled then from Eq. (A2), for any fixed $\vec{y} \in \mathbb{R}^m$, as

a function of \vec{z} the conditional pdf $\mathcal{F}(\vec{z}|\vec{y})$ is proportional to $f(\Psi^{-1}(\vec{z}, \vec{y}))$. Thus, one can detect that the DF $f(\vec{w})$ is stationary, or a cut of a stationary DF, by showing that the *conditional* pdf $\mathcal{F}(\vec{z}|\vec{y})$ is constant for \vec{z} in $\Omega_z(\vec{y})$, at any fixed $\vec{y} \in \mathbb{R}^m$. We show now that this is equivalent to our minimum-entropy principle.

A pdf supported on a fixed bounded region of \mathbb{R}^{6-m} is uniform if, and only if, it has maximal entropy. In this case, $\mathcal{F}(\vec{z}|\vec{y}) = 1/V_z(\vec{y})$, where $V_z(\vec{y})$ is the volume of the maximum allowed support $\Omega_z(\vec{y})$ of $\mathcal{F}(\vec{z}|\vec{y})$, and from Eq. (A5),

$$S(\mathcal{F}(\cdot|\vec{y})) = -\ln \frac{1}{V_z(\vec{y})} = \ln V_z(\vec{y}) .$$

Thus, given a fixed DF f on \mathbb{R}^6 , the expected value $\mathbb{E}_{\vec{y}}[S(\mathcal{F}(\cdot|\vec{y}))]$ in Eq. (A4) is bounded from above by

$$\mathbb{E}_{\vec{y}}[\ln V_z(\vec{y})] = \int_{-\infty}^{\infty} F(\vec{y}) \ln V_z(\vec{y}) d^m \vec{y}$$

and $\mathbb{E}_{\vec{y}}[S(\mathcal{F}(\cdot|\vec{y}))]$ reaches this value when the $\mathcal{F}(\cdot|\vec{y})$ are uniform in their maximum allowed supports. Thus,

$$\mathbb{E}_{\vec{y}}[\ln V_z(\vec{y})] - \mathbb{E}_{\vec{y}}[S(\mathcal{F}(\cdot|\vec{y}))] \geq 0 .$$

Using Eq. (A4),

$$\begin{aligned} \mathbb{E}_{\vec{y}}[\ln V_z(\vec{y})] - S(f) + \mathbb{E}[\ln |J_{\Psi^{-1}}|] + S(F(\vec{y})) &\geq 0 \\ \mathbb{E}[\ln \tilde{V}] + S(F(\vec{y})) &\geq S(f) , \end{aligned}$$

where the random variable \tilde{V} is defined by

$$\tilde{V}(\vec{z}, \vec{y}) \doteq |J_{\Psi^{-1}}(\vec{z}, \vec{y})| V_z(\vec{y}) . \quad (\text{A6})$$

Therefore, by construction, the quantity

$$\mathbb{E}(\ln \tilde{V}) + S(F(\vec{y})) \quad (\text{A7})$$

is bounded from below by $S(f)$ and reaches this value if, and only if, all $\mathcal{F}(\cdot|\vec{y})$ are uniform in their maximum allowed supports. By assumption 2., we have:

$$\mathbb{E}[\ln \tilde{V}] = \mathbb{E}_{\vec{y}}[\ln g(\vec{y})] ,$$

where $g(\vec{y}) = |J_{\Psi^{-1}}(\vec{y})| V_z(\vec{y})$ is the ‘‘density of states’’ at $\vec{y} \in \mathbb{R}^m$. Similar to $F(\vec{y})$, the density of states $g(\vec{y})$ is independent of the particular transformation Ψ in respect to the remaining variables \vec{z} . In fact, we can assume that there is a partial transformation $\tilde{\Psi}$ over the \vec{z} coordinates such that the total transformation has $|J_{\Psi^{-1}}(\vec{z}, \vec{y})| = |J_{\Psi^{-1}}(\vec{y})|$,

$$g(\vec{y}) = |J_{\Psi^{-1}}(\vec{y})| V_z(\vec{y}) = \int_{\Omega_z(\vec{y})} |J_{\Psi^{-1}}(\vec{y})| d^{6-m} \vec{z} = \int_{\tilde{\Omega}_z(\vec{y})} |J_{\Psi^{-1}}(\vec{y})| \frac{|J_{\tilde{\Psi}^{-1}}(\vec{z}, \vec{y})|}{|J_{\Psi^{-1}}(\vec{y})|} d^{6-m} \vec{z} = \int_{\tilde{\Omega}_z(\vec{y})} |J_{\tilde{\Psi}^{-1}}(\vec{z}, \vec{y})| d^{6-m} \vec{z} ,$$

where $\tilde{\Omega}_z(\vec{y})$ is the maximum allowed support of the remaining variables under the second transformation. Thus, the density of states can be generalized for a transformation of coordinates that does *not* satisfy assumption 2. as

$$g(\vec{y}) \doteq \int_{\Omega_z(\vec{y})} |J_{\Psi^{-1}}(\vec{z}, \vec{y})| d^{6-m} \vec{z} . \quad (\text{A8})$$

With this, we can finally relax condition 2. Hence, we proved, under the assumption 1. only, that the quantity

$$\mathbb{E}_{\vec{y}}[\ln g(\vec{y})] + S(F(\vec{y}))$$

is bounded from below by $S(f)$ and reaches this value if, and only if, $f(\Psi^{-1}(\vec{z}, \vec{y}))$ is constant for \vec{z} in $\Omega_z(\vec{y})$.

Consider now a family $\Psi_{\vec{p}}$, $\vec{p} \in P$, of transformations of coordinates in \mathbb{R}^6 satisfying assumption 1., where \vec{p} stands for generic parameters of the potential. We think of $\Psi_{\vec{p}}$ as the set of transformations leading to integrals of motion evaluated in all trial potentials. For some fixed $m < 6$, define $\vec{y}_{\vec{p}}$ by the last m components of $\Psi_{\vec{p}}$, as above. Suppose, as before, that, for all $\vec{p} \in P$ and $\vec{y} \in \mathbb{R}^m$, the maximum allowed support of the pdf's $\mathcal{F}_{\vec{p}}(\cdot|\vec{y})$ is some bounded region $\Omega_z(\vec{p}, \vec{y})$ of \mathbb{R}^{6-m} , which now can also depend on \vec{p} . If, for some $\vec{p}_0 \in P$, the DF f is stationary (phase-mixed), or a cut of a stationary DF, we can find this particular \vec{p}_0 by minimizing with respect to \vec{p} the quantity

$$S_Y \doteq \mathbb{E}_{\vec{y}}[\ln g_{\vec{p}}(\vec{y})] + S(F(\vec{y})) = - \int F(\vec{y}) \ln \left[\frac{F(\vec{y})}{g_{\vec{p}}(\vec{y})} \right] d^m \vec{y} . \quad (\text{A9})$$

We emphasize that S_Y incorporates the density of states $g_{\vec{p}}(\vec{y})$ and thus differs from $S(F(\vec{y}))$. We now show particular cases in terms of energy, angular momentum and actions, making contact with Sec. 3.

A.1. Spherical and isotropic systems

For spherically symmetric systems with isotropic velocities, we use spherical coordinates, in terms of solid angles ω_r and ω_v , with Jacobian determinant $\partial(\vec{r}, \vec{v})/\partial(r, v, \omega_r, \omega_v) = r^2 v^2$. For a given central potential $\phi_{\vec{p}}(r)$, the energy being $E = v^2/2 + \phi_{\vec{p}}(r)$, the Jacobian determinant for $(r, E) \rightarrow (r, v)$ is $\partial(r, v)/\partial(r, E) = 1/\sqrt{2(E - \phi_{\vec{p}}(r))} = 1/v$. Thus,

$$|J_{\Psi_{\vec{p}}}| = \frac{\partial(\vec{r}, \vec{v})}{\partial(r, E, \varpi_r, \varpi_v)} = \frac{\partial(\vec{r}, \vec{v})}{\partial(r, v, \varpi_r, \varpi_v)} \frac{\partial(r, v)}{\partial(r, E)} = r^2 \sqrt{2(E - \phi_{\vec{p}}(r))}.$$

Let $r_m(E)$ be the maximum radius for a particle with energy E . From Eq. (A8), the density of states at fixed E is:

$$g_{\vec{p}}(E) = \int_{(r, \omega_r, \omega_v) \in \Omega_z(E)} r^2 \sqrt{2(E - \phi_{\vec{p}}(r))} dr d\omega_r d\omega_v = (4\pi)^2 \int_0^{r_m(E)} r^2 \sqrt{2(E - \phi_{\vec{p}}(r))} dr.$$

From (A9), our minimum-entropy principle translates into minimizing, with respect to the parameters \vec{p} ,

$$S_E \doteq - \int F(E) \ln \left[\frac{F(E)}{g_{\vec{p}}(E)} \right] dE,$$

where $F(E)$ is the pdf for the energy – c.f. Eq. (17). Note that not only $g_{\vec{p}}$, but also $F(E)$ depends on \vec{p} , via $\phi_{\vec{p}}$.

A.2. Spherical and anisotropic systems

For a spherical system with anisotropic velocity distribution, we let it depend on v_t and v_r , the tangential and radial velocities, respectively. The phase space coordinate (\vec{r}, \vec{v}) is a function of r , the solid angle ω_r , v_r and v_t , as well as a planar angle φ_v referring to the tangent direction of the velocity, i.e. we use cylindrical coordinates for the velocity \vec{v} , with its vertical axis along \vec{r} . For this transformation of coordinates we have $\partial(\vec{r}, \vec{v})/\partial(r, v_r, v_t, \omega_r, \varphi_v) = r^2 v_t$. With the angular momentum $L = r v_t$, and $v^2 = v_t^2 + v_r^2$, we have $v_r = \pm \sqrt{2(E - \phi_{\vec{p}}(r)) - L^2/r^2}$. Thus, the Jacobian determinant of the transformation $(E, L) \rightarrow (v_r, v_t)$ is $\partial(v_r, v_t)/\partial(E, L) = \mp 1 / \left[r \sqrt{2(E - \phi_{\vec{p}}(r)) - L^2/r^2} \right]$. Hence,

$$|J_{\Psi_{\vec{p}}}| = \frac{\partial(\vec{r}, \vec{v})}{\partial(r, E, L, \varpi_r, \varphi_v)} = \frac{\partial(\vec{r}, \vec{v})}{\partial(r, v_r, v_t, \varpi_r, \varphi_v)} \frac{\partial(v_r, v_t)}{\partial(E, L)} = \mp \frac{L}{\sqrt{2(E - \phi_{\vec{p}}(r)) - L^2/r^2}}.$$

From Eq. (A8), the density of states in this case is $g_{\vec{p}}(E, L) = 8\pi^2 L T_r(E, L)$ – c.f. Eqs. (23)-(24). As before, from (A9) the minimum entropy principle refers to minimizing

$$S_{EL} \doteq - \int F(E, L) \ln \left[\frac{F(E, L)}{g_{\vec{p}}(E, L)} \right] dE dL,$$

where $F(E, L)$ is the joint pdf for the energy and angular momentum – c.f. Eq. (21).

A.3. Generic integrable potentials - action variables

If $\Psi_{\vec{p}}$ is a canonical transformation, $|J_{\Psi_{\vec{p}}^{-1}}| = 1$. For instance, if $\Psi_{\vec{p}}$ refer to action-angle variables, $\vec{y}_{\vec{p}}$ being actions, then, in a full-sky survey, i.e. in the absence of any geometric cuts, from Eq. (A8):

$$g_{\vec{p}}(\vec{y}) = \tilde{V}_{\vec{p}}(\vec{y}) = (2\pi)^3$$

From Eq. (A9), our minimum-entropy principle is equivalent to minimizing

$$S_{\vec{J}} \doteq - \int F(\vec{J}) \ln \left[\frac{F(\vec{J})}{(2\pi)^3} \right] d\vec{J},$$

where $F(\vec{J})$ is the joint pdf for the actions – c.f. Eq. (27).

More generally, in the presence of geometrical cuts,

$$g_{\vec{p}}(\vec{y}) \rightarrow g_{\vec{p}}(\vec{y}) A_{\vec{p}}(\vec{y}),$$

where the random variable $0 < A_{\vec{p}} \leq 1$ only depends on \vec{y} (integrals) and refers to the portion of the remaining variables corresponding to stars lying within the survey footprint, at fixed integral. Hence, in the presence of geometric cuts and when using actions, our minimum entropy principle is equivalent to minimizing

$$S_{\vec{J}} = - \int F(\vec{J}) \ln \left[\frac{F(\vec{J})}{(2\pi)^3 A_{\vec{p}}(\vec{J})} \right] d\vec{J}. \quad (\text{A10})$$

B. COULD WE MAXIMIZE THE ENTROPY IN ANGLE-SPACE?

Since the angle distribution is uniform for a phase-mixed sample, one might try to recover the potential by maximizing an entropy using angles. In Sec. 2, we motivated our method by connecting the maximum-likelihood principle with a minimum-entropy one. This already suggests *minimizing* an entropy using integrals, as opposed to *maximizing* one using the remaining variables. Since these live in higher dimensions for the cases $f(E)$ and $f(E, L)$, it would not be helpful to use those variables, so for this discussion we focus on angles and actions, which both live in $d = 3$. We show why we do not expect a maximum-entropy in angle-space to work.

As we demonstrate in Appendix A, writing the DF as $f(\vec{\theta}, \vec{J}) = \mathcal{F}(\vec{\theta}|\vec{J})F(\vec{J})$, we get $S(f) = S(F(\vec{J})) + \mathbb{E}_{\vec{J}} [S(\mathcal{F}(\cdot|\vec{J}))]$, where we have set $|J_{\Psi-1}| = 1$ in Eq. (A4), $F(\vec{J})$ is the action's pdf and $S(\mathcal{F}(\cdot|\vec{J}))$ is the entropy of the conditional pdfs – Eq. (A5). The maximum value of this last term, achieved in the potential where the sample is phase-mixed, is $\mathbb{E} [\ln V_{\vec{\theta}}]$, where $V_{\vec{\theta}}(\vec{J}) = (2\pi)^3 A(\vec{J})$ is the volume of the angles' support (density of states). In a full-sky survey, $A(\vec{J}) = 1$, and $0 < A(\vec{J}) < 1$ in the presence of geometric cuts. This maximum value depends on the potential and needs to join the optimization. Since we can calculate $V_{\vec{\theta}}(\vec{J})$ for each model, and $S(f)$ is invariant, the correct potential is recovered if and only if $S_{\vec{J}}$ is minimum – see Eq. (A10).

On the other hand, in trying to constrain the potential by maximizing the entropy in angle-space, we would separate the DF as $f(\vec{\theta}, \vec{J}) = \mathcal{F}(\vec{J}|\vec{\theta})F(\vec{\theta})$, which implies

$$S(f) = S(F(\vec{\theta})) + \mathbb{E}_{\vec{\theta}} [S(\mathcal{F}(\cdot|\vec{\theta}))],$$

where now $F(\vec{\theta})$ is the angles' pdf and $S(\mathcal{F}(\cdot|\vec{\theta}))$ is the entropy of the conditional pdfs. Although not easily justified, we could conjecture that this last term is minimized in the potential where the sample is phase-mixed, and that, as before, this depends on the potential and should thus join the optimization. However, in this case we do not know what this value should be and do not know which exact quantity to maximize.

In principle, one might try simply maximizing the entropy of the marginal pdf, $S(F(\vec{\theta}))$, but we show two examples suggesting that this would fail. Let us consider an admittedly artificial (1+1)D toy model with DF

$$f(\theta, J) = \frac{1}{\pi} [\delta(\theta \leq \pi)\delta(J \leq 0) + \delta(\theta > \pi)\delta(J > 0)],$$

where $\delta(\mathcal{P}) = 1$ when \mathcal{P} is true, and $\delta(\mathcal{P}) = 0$ otherwise, and $-1/2 \leq J \leq 1/2$. In words, for negative actions, half of the angle maximum allowed support $\Omega_z(J) = [0, 2\pi]$ is uniformly distributed, and for positive actions the other half is. At fixed J , this DF is not constant as a function of θ in $\Omega_z(J)$. Nevertheless, the marginal $F(\theta) = \int f(\theta, J) dJ$ is uniform, and $F(\theta)$ has maximum entropy. Thus, maximizing $S(F(\theta))$ generally fails to reject non-stationary DFs.

As a second example, let $\Omega_z(J) = [0, 4\pi|J|]$ for $-1/2 \leq J \leq 1/2$ and $\Omega_z(J) = [0, 2\pi]$ when $|J| > 1/2$. This choice is to be understood as a “toy model” in the presence of a geometric cut. Define the DF by

$$f(\theta, J) = \frac{1}{\pi} \delta(\theta \in \Omega_z(J)) \delta(|J| \leq 1/2).$$

This DF $f(\theta, J)$ is now uniform in angles. However, the marginal pdf in this case is not uniform:

$$F(\theta) = \int f(\theta, J) dJ = \frac{1}{\pi} \left(1 - \frac{\theta}{2\pi} \right),$$

and thus its entropy is not maximum and maximizing $S(F(\theta))$ also generally fails to detect stationary DFs.

REFERENCES

- Ajgl, J., & Šimandl, M. 2011, IFAC Proceedings, 44, 11991, doi: <https://doi.org/10.3182/20110828-6-IT-1002.01404>
- Akaike, H. 1992, Information Theory and an Extension of the Maximum Likelihood Principle (New York, NY: Springer New York), 610–624, doi: [10.1007/978-1-4612-0919-5_38](https://doi.org/10.1007/978-1-4612-0919-5_38)

- Ao, Z., & Li, J. 2023, *Artificial Intelligence*, 322, 103954, doi: <https://doi.org/10.1016/j.artint.2023.103954>
- Bahcall, J. N., & Tremaine, S. 1981, *ApJ*, 244, 805, doi: [10.1086/158756](https://doi.org/10.1086/158756)
- Banik, U., Weinberg, M. D., & van den Bosch, F. C. 2022, *ApJ*, 935, 135, doi: [10.3847/1538-4357/ac7ff9](https://doi.org/10.3847/1538-4357/ac7ff9)
- Barbieri, L., Di Cintio, P., Giachetti, G., Simon-Petit, A., & Casetti, L. 2022, *MNRAS*, 512, 3015, doi: [10.1093/mnras/stac477](https://doi.org/10.1093/mnras/stac477)
- Beaumont, M. A., Zhang, W., & Balding, D. J. 2002, *Genetics*, 162, 2025, doi: [10.1093/genetics/162.4.2025](https://doi.org/10.1093/genetics/162.4.2025)
- Beirlant, J., Dudewicz, E., Gyor, L., & Meulen, E. 1997, *International Journal of Mathematical and Statistical Sciences*, 6
- Beloborodov, A. M., & Levin, Y. 2004, *ApJ*, 613, 224, doi: [10.1086/422908](https://doi.org/10.1086/422908)
- Beraldo e Silva, L., de Siqueira Pedra, W., Sodré, L., Perico, E. L. D., & Lima, M. 2017, *ApJ*, 846, 125, doi: [10.3847/1538-4357/aa876e](https://doi.org/10.3847/1538-4357/aa876e)
- Beraldo e Silva, L., de Siqueira Pedra, W., & Valluri, M. 2019a, *ApJ*, 872, 20, doi: [10.3847/1538-4357/aaf8a7](https://doi.org/10.3847/1538-4357/aaf8a7)
- Beraldo e Silva, L., de Siqueira Pedra, W., Valluri, M., Sodré, L., & Bru, J.-B. 2019b, *ApJ*, 870, 128, doi: [10.3847/1538-4357/aaf397](https://doi.org/10.3847/1538-4357/aaf397)
- Berrett, T. B., Samworth, R. J., & Yuan, M. 2019, *The Annals of Statistics*, 47, pp. 288
- Besla, G., Kallivayalil, N., Hernquist, L., et al. 2007, *ApJ*, 668, 949, doi: [10.1086/521385](https://doi.org/10.1086/521385)
- Biau, G., & Devroye, L. 2015, *Lectures on the Nearest Neighbor Method*, 1st edn. (Springer Publishing Company, Incorporated)
- Binney, J. 2012, *MNRAS*, 426, 1324, doi: [10.1111/j.1365-2966.2012.21757.x](https://doi.org/10.1111/j.1365-2966.2012.21757.x)
- Binney, J., & Petrou, M. 1985, *MNRAS*, 214, 449, doi: [10.1093/mnras/214.4.449](https://doi.org/10.1093/mnras/214.4.449)
- Binney, J., & Tremaine, S. 2008, *Galactic Dynamics: Second Edition*, Princeton Series in Astrophysics (Princeton University Press)
- Chang, J. T., & Pollard, D. 1997, *Statistica Neerlandica*, 51, 287, doi: <https://doi.org/10.1111/1467-9574.00056>
- Charzyńska, A., & Gambin, A. 2015, *Entropy*, 18, 13, doi: [10.3390/e18010013](https://doi.org/10.3390/e18010013) FILE:/proj/ads/abstracts/
- Cooper, A. P., Kaposov, S. E., Allende Prieto, C., et al. 2023, *ApJ*, 947, 37, doi: [10.3847/1538-4357/acb3c0](https://doi.org/10.3847/1538-4357/acb3c0)
- Correa Magnus, L., & Vasiliev, E. 2022, *MNRAS*, 511, 2610, doi: [10.1093/mnras/stab3726](https://doi.org/10.1093/mnras/stab3726)
- Cranmer, K., Brehmer, J., & Louppe, G. 2020, *Proceedings of the National Academy of Science*, 117, 30055, doi: [10.1073/pnas.1912789117](https://doi.org/10.1073/pnas.1912789117)
- Cui, X.-Q., Zhao, Y.-H., Chu, Y.-Q., et al. 2012, *Research in Astronomy and Astrophysics*, 12, 1197, doi: [10.1088/1674-4527/12/9/003](https://doi.org/10.1088/1674-4527/12/9/003)
- De Silva, G. M., Freeman, K. C., Bland-Hawthorn, J., et al. 2015, *MNRAS*, 449, 2604, doi: [10.1093/mnras/stv327](https://doi.org/10.1093/mnras/stv327)
- Deason, A. J., Erkal, D., Belokurov, V., et al. 2021, *MNRAS*, 501, 5964, doi: [10.1093/mnras/staa3984](https://doi.org/10.1093/mnras/staa3984)
- Dehnen, W. 2005, *MNRAS*, 360, 892, doi: [10.1111/j.1365-2966.2005.09099.x](https://doi.org/10.1111/j.1365-2966.2005.09099.x)
- Erkal, D., Deason, A. J., Belokurov, V., et al. 2021, *MNRAS*, 506, 2677, doi: [10.1093/mnras/stab1828](https://doi.org/10.1093/mnras/stab1828)
- Evans, N. W., & An, J. 2005, *MNRAS*, 360, 492, doi: [10.1111/j.1365-2966.2005.09078.x](https://doi.org/10.1111/j.1365-2966.2005.09078.x)
- Ewart, R. J., Nastac, M. L., & Schekochihin, A. A. 2023, *Journal of Plasma Physics*, 89, 905890516, doi: [10.1017/S0022377823000983](https://doi.org/10.1017/S0022377823000983)
- Fouvry, J.-B., Hamilton, C., Rozier, S., & Pichon, C. 2021, *MNRAS*, 508, 2210, doi: [10.1093/mnras/stab2596](https://doi.org/10.1093/mnras/stab2596)
- Gaia Collaboration, et al. 2016, *A&A*, 595, A1, doi: [10.1051/0004-6361/201629272](https://doi.org/10.1051/0004-6361/201629272)
- Garavito-Camargo, N., Besla, G., Laporte, C. F. P., et al. 2021, *ApJ*, 919, 109, doi: [10.3847/1538-4357/ac0b44](https://doi.org/10.3847/1538-4357/ac0b44)
- Green, G. M., Ting, Y.-S., & Kamdar, H. 2023, *ApJ*, 942, 26, doi: [10.3847/1538-4357/aca3a7](https://doi.org/10.3847/1538-4357/aca3a7)
- Hahn, C., Vakili, M., Walsh, K., et al. 2017, *MNRAS*, 469, 2791, doi: [10.1093/mnras/stx894](https://doi.org/10.1093/mnras/stx894)
- Han, J., Wang, W., Cole, S., & Frenk, C. S. 2016, *MNRAS*, 456, 1003, doi: [10.1093/mnras/stv2707](https://doi.org/10.1093/mnras/stv2707)
- Harris, C. R., Millman, K. J., van der Walt, S. J., et al. 2020, *Nature*, 585, 357, doi: [10.1038/s41586-020-2649-2](https://doi.org/10.1038/s41586-020-2649-2)
- Hattori, K., Valluri, M., & Vasiliev, E. 2021, *MNRAS*, 508, 5468, doi: [10.1093/mnras/stab2898](https://doi.org/10.1093/mnras/stab2898)
- Henon, M. 1959, *Annales d'Astrophysique*, 22, 126
- Hernquist, L. 1990, *ApJ*, 356, 359, doi: [10.1086/168845](https://doi.org/10.1086/168845)
- Jiang, B. 2018, in *Proceedings of Machine Learning Research*, Vol. 84, Proceedings of the Twenty-First International Conference on Artificial Intelligence and Statistics, ed. A. Storkey & F. Perez-Cruz (PMLR), 1711–1721. <https://proceedings.mlr.press/v84/jiang18a.html>
- Kullback, S. 1968, *Information theory and statistics* (Dover publications)
- Leonenko, N., Pronzato, L., & Savani, V. 2008, *The Annals of Statistics*, 36, 2153, doi: [10.1214/07-AOS539](https://doi.org/10.1214/07-AOS539)
- Levin, Y., Pakter, R., Rizzato, F. B., Teles, T. N., & Benetti, F. P. C. 2014, *PhR*, 535, 1, doi: [10.1016/j.physrep.2013.10.001](https://doi.org/10.1016/j.physrep.2013.10.001)
- Li, Z., Han, J., Wang, W., et al. 2024, *arXiv e-prints*, arXiv:2408.11414, doi: [10.48550/arXiv.2408.11414](https://doi.org/10.48550/arXiv.2408.11414)

- Lombardi, D., & Pant, S. 2016, *PhRvE*, 93, 013310, doi: [10.1103/PhysRevE.93.013310](https://doi.org/10.1103/PhysRevE.93.013310)
- Lynden-Bell, D. 1967, *MNRAS*, 136, 101, doi: [10.1093/mnras/136.1.101](https://doi.org/10.1093/mnras/136.1.101)
- Magorrian, J. 2014, *MNRAS*, 437, 2230, doi: [10.1093/mnras/stt2031](https://doi.org/10.1093/mnras/stt2031)
- Majewski, S. R., Schiavon, R. P., Frinchaboy, P. M., et al. 2017, *AJ*, 154, 94, doi: [10.3847/1538-3881/aa784d](https://doi.org/10.3847/1538-3881/aa784d)
- Martin, O., Kumar, R., & Lao, J. 2021, *Bayesian Modeling and Computation in Python*, Chapman & Hall/CRC Texts in Statistical Science (CRC Press). <https://books.google.com/books?id=0UtSEAAAQBAJ>
- McMillan, P. J. 2017, *MNRAS*, 465, 76, doi: [10.1093/mnras/stw2759](https://doi.org/10.1093/mnras/stw2759)
- McMillan, P. J., & Binney, J. 2012, *MNRAS*, 419, 2251, doi: [10.1111/j.1365-2966.2011.19879.x](https://doi.org/10.1111/j.1365-2966.2011.19879.x)
- McMillan, P. J., & Binney, J. J. 2013, *MNRAS*, 433, 1411, doi: [10.1093/mnras/stt814](https://doi.org/10.1093/mnras/stt814)
- Modak, S., & Hamilton, C. 2023, *MNRAS*, 524, 3102, doi: [10.1093/mnras/stad2073](https://doi.org/10.1093/mnras/stad2073)
- Nastac, M. L., Ewart, R. J., Sengupta, W., et al. 2024, *PhRvE*, 109, 065210, doi: [10.1103/PhysRevE.109.065210](https://doi.org/10.1103/PhysRevE.109.065210)
- Nyquist, H. 1928, *Transactions of the American Institute of Electrical Engineers*, 47, 617, doi: [10.1109/T-AIEE.1928.5055024](https://doi.org/10.1109/T-AIEE.1928.5055024)
- Peñarrubia, J., Kuposov, S. E., & Walker, M. G. 2012, *ApJ*, 760, 2, doi: [10.1088/0004-637X/760/1/2](https://doi.org/10.1088/0004-637X/760/1/2)
- Petersen, M. S., & Peñarrubia, J. 2021, *Nature Astronomy*, 5, 251, doi: [10.1038/s41550-020-01254-3](https://doi.org/10.1038/s41550-020-01254-3)
- Plummer, H. C. 1911, *MNRAS*, 71, 460, doi: [10.1093/mnras/71.5.460](https://doi.org/10.1093/mnras/71.5.460)
- Price-Whelan, A. M., Hogg, D. W., Johnston, K. V., et al. 2021, *ApJ*, 910, 17, doi: [10.3847/1538-4357/abe1b7](https://doi.org/10.3847/1538-4357/abe1b7)
- Rehemtulla, N., Valluri, M., & Vasiliev, E. 2022, *MNRAS*, 511, 5536, doi: [10.1093/mnras/stac400](https://doi.org/10.1093/mnras/stac400)
- Sanders, J. L., & Binney, J. 2016, *MNRAS*, 457, 2107, doi: [10.1093/mnras/stw106](https://doi.org/10.1093/mnras/stw106)
- Sanderson, R. E., Helmi, A., & Hogg, D. W. 2015, *ApJ*, 801, 98, doi: [10.1088/0004-637X/801/2/98](https://doi.org/10.1088/0004-637X/801/2/98)
- Schälte, Y., Klinger, E., Alamoudi, E., & Hasenauer, J. 2022, *Journal of Open Source Software*, 7, 4304, doi: [10.21105/joss.04304](https://doi.org/10.21105/joss.04304)
- Shannon, C. 1949, *Proceedings of the IRE*, 37, 10, doi: [10.1109/JRPROC.1949.232969](https://doi.org/10.1109/JRPROC.1949.232969)
- Silverman, B. W. 1986, *Density estimation for statistics and data analysis* (Chapman and Hall)
- Sisson, S., Fan, Y., & Beaumont, M. 2018, *Handbook of Approximate Bayesian Computation*, ISSN (CRC Press)
- Sisson, S. A., Fan, Y., & Tanaka, M. M. 2007, *Proceedings of the National Academy of Sciences*, 104, 1760, doi: [10.1073/pnas.0607208104](https://doi.org/10.1073/pnas.0607208104)
- Ting, Y.-S., Rix, H.-W., Bovy, J., & van de Ven, G. 2013, *MNRAS*, 434, 652, doi: [10.1093/mnras/stt1053](https://doi.org/10.1093/mnras/stt1053)
- Tremaine, S. 2018, *MNRAS*, 477, 946, doi: [10.1093/mnras/sty737](https://doi.org/10.1093/mnras/sty737)
- Tremaine, S., Hénon, M., & Lynden-Bell, D. 1986, *MNRAS*, 219, 285, doi: [10.1093/mnras/219.2.285](https://doi.org/10.1093/mnras/219.2.285)
- Trick, W. H., Bovy, J., & Rix, H.-W. 2016, *ApJ*, 830, 97, doi: [10.3847/0004-637X/830/2/97](https://doi.org/10.3847/0004-637X/830/2/97)
- Valluri, M., Chabanier, S., Irsic, V., et al. 2022, *arXiv e-prints*, arXiv:2203.07491, doi: [10.48550/arXiv.2203.07491](https://doi.org/10.48550/arXiv.2203.07491)
- Vasiliev, E. 2019, *MNRAS*, 482, 1525, doi: [10.1093/mnras/sty2672](https://doi.org/10.1093/mnras/sty2672)
- Virtanen, P., Gommers, R., Oliphant, T. E., et al. 2020, *Nature Methods*, 17, 261, doi: [10.1038/s41592-019-0686-2](https://doi.org/10.1038/s41592-019-0686-2)
- Wasserman, L. 2010, *All of statistics : a concise course in statistical inference* (New York: Springer). <https://link.springer.com/book/10.1007/978-0-387-21736-9>
- Watkins, L. L., Evans, N. W., & An, J. H. 2010, *MNRAS*, 406, 264, doi: [10.1111/j.1365-2966.2010.16708.x](https://doi.org/10.1111/j.1365-2966.2010.16708.x)
- Wolsztynski, E., Thierry, E., & Pronzato, L. 2005, *Signal Processing*, 85, 937, doi: <https://doi.org/10.1016/j.sigpro.2004.11.028>
- Zhdankin, V. 2022, *Physical Review X*, 12, 031011, doi: [10.1103/PhysRevX.12.031011](https://doi.org/10.1103/PhysRevX.12.031011)
- . 2023, *Journal of Physics A Mathematical General*, 56, 385002, doi: [10.1088/1751-8121/acf175](https://doi.org/10.1088/1751-8121/acf175)
- Zwicky, F. 1933, *Helvetica Physica Acta*, 6, 110